Journal Pre-proof

A methodology to simulate interior and intermediate ballistics with dynamic mesh technique and lumped parameter code

G. Guermonprez, T. Gaillard, J. Dupays, J. Anthoine, R. Demarthon

PII: S2214-9147(25)00060-1

DOI: https://doi.org/10.1016/j.dt.2025.02.021

Reference: DT 1605

To appear in: *Defence Technology*

Received Date: 29 November 2024

Revised Date: 24 January 2025

Accepted Date: 24 February 2025

Please cite this article as: Guermonprez G, Gaillard T, Dupays J, Anthoine J, Demarthon R, A methodology to simulate interior and intermediate ballistics with dynamic mesh technique and lumped parameter code, *Defence Technology*, https://doi.org/10.1016/j.dt.2025.02.021.

A methodology to simulate interior and intermediate ballistics with dynamic mesh technique and lumped parameter code

G. Guermonprez[a,*], T. Gaillard[a], J. Dupays[a], J. Anthoine[a], R. Demarthon[b]

[a]DMPE, ONERA, Université Paris Saclay, 91120, Palaiseau, France

[b]DGA Techniques Terrestres, Rocade Est – Echangeur de Guerry, 18021 Bourges Cedex, France

*Corresponding author. E-mail address: gabin.guermonprez@onera.fr

A methodology to simulate interior and intermediate ballistics with Dynamic Mesh Technique and lumped parameter code

Abstract

The aim of this paper is to simulate and study the early moments of the reactive ballistics of a large caliber projectile fired from a gun, combining 0D and 2D axisymmetric Computational Fluid Dynamics (CFD) approaches. First, the methodology is introduced with the development of an interior ballistics (IB) lumped parameter code (LPC), integrating an original image processing method for calculating the specific regression of propellant grains that compose the gun propellant. The ONERA CFD code CEDRE, equipped with a Dynamic Mesh Technique (DMT), is then used in conjunction with the developed LPC to build a dedicated methodology to calculate IB. First results obtained on the AGARD gun and 40 mm gun test cases are in a good agreement with the existing literature. CEDRE is also used to calculate intermediate ballistics (first milliseconds of free flight of the projectile) with a multispecies and reactive approach either starting from the gun muzzle plane or directly following IB. In the latter case, an inverse problem involving a Latin hypercube sampling method is used to find a gun propellant configuration that allows the projectile to reach a given exit velocity and base pressure when IB ends. The methodology developed in this work makes it possible to study the flame front of the intermediate flash and depressurization that occurs in a base bleed (BB) channel at the gun muzzle. Average pressure variations in the BB channel during depressurization are in good agreement with literature.

Keywords: Intermediate ballistics; Interior Ballistics (IB); Lumped Parameter Code (LPC); Form Function; Dynamic Mesh

Abbreviations

ALE	Arbitrary Lagrangian-Eulerian
B7T / B19T	Perforated cylindrical propellant grain (7/19 holes) with composition B (99% of nitrocellulose)
BB	Base Bleed
CFD	Computational Fluid Dynamics
CPU	Central Proccessing Unit
DMT	Dynamic Mesh Technique
EOS	Equation of State
HRR	Heat Release Rate
IB	Interior Ballistics
LPC	Lumped Parameter Code
LS	Level Set
SST	Shear Stress Transport

Nomenclature

A	Shell base section, m²

$A_{\mathrm{grain}}(t), A_{\mathrm{grain},0}$	Cross-section of a gun propellant grain at time t and $t = 0$, m²
b	Covolume, m³/kg
$C_{\mathrm{grain}}(t), C_{\mathrm{grain},0}$	Circumference of the cross-section of a gun propellant grain at time t and t = 0, m
$\mathrm{d}t$	Time step, s
$\mathrm{d}U$	Variation of internal energy of the gun propellant combustion products during dt, J
D_b, D_w	Diameter of a black or white disk, m
D_{grain}	Initial diameter of a gun propellant grain, m
D_{holes}	Diameter of a gun propellant grain holes, m
F_p, F_l	Gun propellant and igniter propellant impetus, J/kg
$l(t), l_0$	Length of a gun propellant grain at time t and $t = 0$, m
L	Pixel side length, m
L_i	Length of the i^{th} segment of an interface between black and white pixels, m
$m_{\mathrm{grain}}(t), m_{\mathrm{grain},0}$	Gun propellant grain mass at time t and $t = 0$, kg
$m_p(t), m_{p,0}, m_l$	Gun propellant mass at time t and $t = 0$, and total mass of the igniter propellant, kg
m_{shell}	Shell mass, kg
n	Number of side pixels of an image
n_{black}	Number of black pixels of an image
N	Gun propellant grain number
N_{points}	Number of points describing an interface
P	Pressure, Pa
$P_{\mathrm{mean}}, P_{\mathrm{base}}, P_{\mathrm{breech}}$	Mean pressure, base pressure and breech pressure, Pa
P_r	Resistant pressure, Pa
r	Regression distance, m
r_{g}	Specific gas constant, J/(kg·K)
R	Image scale factor, m/pixels
S	Total combustion surface of a gun propellant grain, m²
T	Temperature, K
T_{mean}	Mean combustion chamber temperature, K
$T_{\mathrm{f}}, T_{\mathrm{fl}}$	Gun propellant and igniter propellant flame temperature, K
v	Specific volume, m³/kg
v_c	Regression rate from Vieille's law, m/s
V_{c}	Combustion chamber volume, m³
V_g, V_p	Gun propellant combustion products and gun propellant volume, m³
x	Shell longitudinal displacement, m

Y_k	Mass fraction of species *k*
z	Gun propellant burnt mass fraction
α	First Vieille's law coefficient, m/(s·MPa$^{\beta}$)
β	Vieille's law pressure exponent
$\gamma_{\mathrm{p}}, \gamma_{\mathrm{I}}$	Gun propellant combustion products and igniter propellant specific heat ratio
δ_{Losses}	Energy loss term during $\mathrm{d}t$, J
δQ	Energy released by the gun propellant combustion during $\mathrm{d}t$, J
δW	Work extracted from the gun propellant combustion products during dt to set the shell in motion, J
Δt_{ign}	Ignition delay, s
ζ	Grayscale shading factor
μ	Non-tangential disk factor
$\rho_{\mathrm{p}}, \rho_{\mathrm{I}}$	Gun propellant and igniter propellant density, kg/m^3
ϕ	Form function

1. Introduction

The internal ballistics (IB) of a projectile in a gun deals with the time period between the earliest moments of the gun propellant charges combustion in the gun, to the exit of the projectile base from the gun muzzle [1]. The chemical energy contained in the gun propellant is transferred into kinetic energy for the projectile through the combustion of the gun propellant and the release of gun propellant combustion products in the combustion chamber. The following phase is intermediate ballistics and concerns the exit of the projectile from the gun barrel. During this phase, the gun propellant combustion products behind the projectile expand into the atmosphere, generating a strong under-expanded flow [2]. It is during this phase that a base bleed (BB) located at the projectile base can be extinguished due to severe depressurization [3]. The BB is a solid propellant device placed at the base of a shell. It is probably ignited during IB [4] and it generates a low mass flow rate in the shell wake during intermediate and exterior ballistics. This low flow rate modifies the recirculation at the shell base, thus reducing drag [5]. The release of reactive hot combustion products in the shell wake also leads to temperature increase in this area, hence leading to additional pressure increase and drag reduction. A critical temperature must be reached in the shell wake to initiate secondary combustion for better temperature and pressure rise [6]. Therefore, when it comes to using a BB, it is important to be able to simulate IB and intermediate ballistics using realistic approaches.

There are two main classes of code for simulating the IB phase of a gunshot: lumped parameter codes (LPC) and multiphase CFD codes. A very detailed and up-to-date review of these codes can be found in Ref. [7]. Lumped parameter models are based on a description of the thermodynamic behavior of the gun propellant combustion products contained in the combustion chamber behind the projectile, assuming a particular pressure distribution

(Lagrange or Pidduck-Kent [7]) between the breech and the projectile base. On the other hand, codes based on CFD methods solve conservation equations in control volumes composing the mesh of the domain. Eulerian-Eulerian approaches describe the solid and gas phases in an Eulerian formalism. Lagrangian-Eulerian approaches treat the solid phase in a Lagrangian formalism and follow the motion of the solid gun propellant charges composed of small grains.

During IB, the gun propellant grains burn and regress in parallel layers according to the classical assumption. Several types of gun propellant grains exist in literature: cylindrical, spherical, flakes, 7-hole or 19-hole perforated cylinder (B7T and B19T) as examples. These different geometries do not regress in the same way, and as the quantity of released gun propellant combustion products is directly linked to the combustion surface, knowledge of the combustion surface evolution as a function of the burnt gun propellant fraction (form function) is crucial for any IB code. A special effort is made in this article to precisely characterize the regression of these grains. In 1975, Stals [8] developed analytical formulas to calculate form functions for a wide range of grain geometries. Face inhibition and grain slivering are considered. These formulas give very precise results, but their direct applications are also restricted to certain types of geometry. Form functions for geometries with different web (minimum distance to burn) cannot be calculated in this way. Wurster [9] developed a cellular automaton (ICT-Cellular-Combustion-Algorithm) to calculate form functions of 2D complex cross-sectional geometries. Coupled with an LPC, it is then possible to calculate the combustion of gun propellant grains in a closed bomb. In this model, the mass evolution of each cell is influenced by the eight cells in its Moore neighborhood of order 1 (cells in contact with the cell of interest). Wang et al. [10] presented a gun propellant grain regression method based on the Level-Set (LS) formalism mainly used for solid rocket motors. Complex shapes such as finocyl shapes with cracks can be treated. A three-dimensional LS function is defined and the zeros of this function define the points of the burning surface.

Setting the projectile in motion during IB can be handled in different ways. Dynamic mesh methods are often used, such as the chimera method. This method, described in Guerrero's thesis [11], uses a mask linked to the physical boundaries of a dynamic mesh, with points defining the contours of the mask called interpolated points. These points receive the values of the modeled field solutions of the overlapped fixed mesh. Della Pieta and Reynaud [12] use a moving boundary to set the projectile base in motion. At each time step, the closest cell attached to the moving base grows larger. This cell is divided into two cells when its size exceeds a certain threshold. An ALE formulation of the conservation equations is adopted to account for the moving cells. This method is used in MOBIDIC-NG [12], a two-phase 2D axisymmetric IB code.

Several approaches to simulate intermediate ballistics are presented in literature. It is possible to simulate intermediate ballistics alone, by placing the projectile directly at the muzzle of the barrel as done by Zhuo et al. [13], or by placing the projectile at the bottom of the barrel by modeling the preceding IB phase as done by Zhang et al. [14] and Qin et al. [15]. The CFD codes presented in literature are generally developed with the aim of simu-

lating one of the two phases (IB or intermediate ballistics) with dedicated approaches. The multiphase character of IB and the gas-phase reactive character of intermediate ballistics are usually complex to consider in the same code. For example, on the one hand, the FREIN code [16] developed by KNDS Ammo France and the University of Poitiers simulates IB in a two-phase, reactive manner, with a description of the grain form function and inter-phase drag. On the other hand, for intermediate ballistics, FREIN solves Euler's equations with non-miscible and non-reactive gases.

In this paper, IB is modeled in simple way and intermediate ballistics is described in a detailed way. First, the development of an IB LPC with an original, simple and efficient method to compute gun propellant grain regression is presented. An approach to couple this LPC with a CFD code is then introduced. With the LPC, a particular gun propellant configuration can be found using a Latin hypercube sampling method to obtain targeted base pressure and muzzle velocity between IB and intermediate ballistics. Afterwards, IB and then intermediate ballistics with reactive species can be simulated (alone and one after the other) by coupling the LPC, the CFD code and a DMT. Finally, the depressurization of the gun propellant combustion products in an inert BB channel during intermediate ballistics can be characterized.

2. Lumped parameter code (LPC) for IB computation

The idea of developing an LPC is based on the need to have a simple 0D code to calculate IB in order to obtain a reference solution and to support the CFD calculation of the IB phase by CEDRE. While less sophisticated than CFD-based models, the LPC provides reliable results in terms of gun performance at low computational costs. Incorporating additional parameters to account for physical phenomena such as bore resistance, heat losses, and recoil, enhances the precision of the LPC. CEDRE assistance is then achieved through a weak coupling between the LPC and CEDRE (as explained in section

4.2.), which consists of feeding CEDRE with LPC results to guide CEDRE on the correct ballistic trajectory.

2.1. Assumptions of the model

The physical assumptions of the LPC developed in this work are as follows:

(1) The volume of the gun combustion chamber V_c at time *t*, between the breech and the shell base, is separated into a gas volume V_g and a gun propellant volume $V_{\mathrm{p}} = \frac{m_{\mathrm{p}}}{\rho_{\mathrm{p}}}$ as shown in Eq. **Error! Reference source not found.**:

$$V_c = \frac{m_p}{\rho_p} + V_g \tag{1}$$

with ρ_{p} the gun propellant density and m_{p} the gun propellant mass.

(2) The igniter propellant is assumed to have completely burnt and the gun propellant is assumed to ignite at the start of the computation.

(3) Changes in gun propellant grain temperature are not taken into account.

(4) The gases initially present in the chamber solely come from the igniter combustion.

(5) The regression rate v_c of the gun propellant grains depends on the gas pressure P according to Vieille's law

[17-[19] as shown in Eq. **Error! Reference source not found.:**

$$V_{\mathrm{c}} = \frac{m_{\mathrm{p}}}{\rho_{\mathrm{p}}} + V_g \tag{2}$$

v_{c} is given in m/s, α is a coefficient of Vieille's law in m/(s·MPa$^{\beta}$), P is given in MPa and β is the pressure exponent.

(6) The gun propellant flame temperature is supposed to remain constant while the gun propellant is burning.

(7) The gas phase obeys the Noble-Abel equation of state (EOS) as shown in Eq. **Error! Reference source not found.**:

$$P(v - b) = r_{\mathrm{g}} T \tag{3}$$

with v the specific volume, b the covolume, r_g the specific gas constant and T the temperature.

(8) Pressure between the breech and the shell base is distributed according to a Lagrange profile, which is a common hypothesis in IB context. This assumption is explained in section 2.2. Governing equations for the ballistic trajectory.

(9) The gas phase undergoes an adiabatic transformation during IB (no heat loss at the gun walls).

2.2. Governing equations for the ballistic trajectory

The LPC is based on an energy balance applied to the thermodynamic system represented by the gun propellant combustion products contained in the gun combustion chamber. The fundamental Eq. **Error! Reference source not found.** related to this energy balance can be found in the work of Baer and Frankle [19] or in the STANAG 4367 [20].

$$\delta Q = \mathrm{d}U + \delta W + \delta_{\mathrm{Losses}} \tag{4}$$

δQ is the energy released by the gun propellant combustion, $\mathrm{d}U$ is the infinitesimal variation of the internal energy of the gun propellant combustion products, δW is the work extracted from the gun propellant combustion to set the shell in motion and δ_{Losses} is the loss term representing the kinetic energy of the gas and gun propellant grains $E_c^{\mathrm{gaz+propellant}}$, which is introduced in Eq. **Error! Reference source not found.**). Losses due to the resistant forces of the gun walls on the shell are included in the resistant pressure P_{r} introduced in the expression of the base and breech pressure given below in Eq. **Error! Reference source not found.**. All the terms in Eq. **Error! Reference source not found.** are evaluated over an infinitesimal period of time dt and terms introduced below (mass of gun propellant, burnt mass fraction, *Q*, *U*, *W* and Losses) are evaluated at each time step by integrating these terms over the current computational elapsed time. Rewriting Eq. **Error! Reference source not found.** as done in Ref. [19] gives expression **Error! Reference source not found.** for the mean gas temperature T_{mean} at each time step in the combustion chamber:

$$T_{\mathrm{mean}} = \frac{\frac{m_{p_0} z F_p}{\gamma_p - 1} + \frac{m_{\mathrm{I}} F_{\mathrm{I}}}{\gamma_{\mathrm{I}} - 1} - A \int_0^x P_{\mathrm{base}} \mathrm{d}x - \mathrm{Losses}}{\frac{m_{p_0} z F_p}{(\gamma_p - 1) T_{\mathrm{f}}} + \frac{m_{\mathrm{I}} F_{\mathrm{I}}}{(\gamma_{\mathrm{I}} - 1) T_{f_{\mathrm{I}}}}} \tag{5}$$

with m_{p_0} the initial gun propellant mass, z the burnt mass fraction of the gun propellant, F_p and F_I the impetus of the gun propellant and igniter propellant respectively, γ_{p} and γ_{I} the specific heat ratio (averaged over IB) of the gun propellant and igniter propellant combustion products respectively, T_f and T_{fI} the flame temperature of the

gun propellant and igniter propellant respectively, m_{I} the mass of the igniter propellant, A the shell base section, x the longitudinal displacement of the shell ($x = 0$ is set for its initial position) and P_{base} the pressure at the shell base evaluated at each time step. The mean pressure in the combustion chamber P_{mean} is obtained with the Noble-Abel EOS using the mean gas temperature from Eq. **Error! Reference source not found.**. Moreover, Lagrange's assumption [21] is adopted, meaning that the mixture of the gun propellant combustion products and gun propellant grains is homogeneous between the breech and the shell base. With the additional assumptions of null velocity at the breech, shell velocity at the shell base and constant section of the bore, the expressions for the pressures at the base and at the breech can be obtained in Eq. **Error! Reference source not found.** as done in Ref. [21] (appendix A p. 21), also including a balance of pressure forces on the shell.

$$\begin{cases} P_{\mathrm{base}} = \dfrac{3P_{\mathrm{mean}} + \dfrac{Nm_{\mathrm{grain},0}}{m_{\mathrm{shell}}} P_{\mathrm{r}}}{3 + \dfrac{Nm_{\mathrm{grain},0}}{m_{\mathrm{shell}}}} \\ P_{\mathrm{breech}} = P_{\mathrm{base}} + \dfrac{Nm_{\mathrm{grain},0}}{2m_{\mathrm{shell}}} (P_{\mathrm{base}} - P_{\mathrm{r}}) \end{cases} \tag{6}$$

In Eq. **Error! Reference source not found.**, N is the number of gun propellant grains, $m_{\mathrm{grain},0}$ is the initial mass of a gun propellant grain and m_{shell} is the shell mass. Note that P_{r} usually represents all the resisting forces from the bore acting on the shell. In the AGARD gun case, P_{r} is assumed to be constant along the barrel. However, as mentioned in the STANAG 4367 [20], P_{r} is normally higher at the beginning of IB, representing projectile engraving, and then decreases to a nearly constant value, representing barrel friction on the shell. P_{r} therefore takes the form of a piecewise linear function of the distance travelled by the shell through the barrel. Additional discussion of P_{r} modelling is provided in section 3.2. .

Lagrange's assumption (see Ref. [21]) also allows expressing the energy loss represented by the kinetic energy of the mixture of the gun propellant combustion products and gun propellant grains through Eq. **Error! Reference source not found.**:

$$\text{Losses} = E_c^{\text{gaz+propellant}} = \lambda_1 \frac{m_{p_0}}{m_{\mathrm{shell}}} E_c^{\mathrm{shell}} \tag{7}$$

with $\lambda_1 = 1/3$, the first Piobert's coefficient and E_c^{shell} the kinetic energy of the shell.

2.3. Governing equations for the gun propellant grain regression

This section deals with an original method for calculating the regression of gun propellant grains. This method is the subject of a separate "regression" routine from the main "ballistics" routine of the LPC code written in Python. During an LPC calculation, communication between the two routines takes place at each time step. The pressure-dependent regression thicknesses obtained from the ballistics routine are passed to the regression routine to determine the next combustion surface. Conversely, the combustion surface from the regression routine is passed to the ballistics routine to determine the next mass flow rate of gun propellant combustion products that will affect the pressure evolution in the combustion chamber. Only perforated cylindrical grains with 7 or 19 holes (B7T or B19T) are considered here for the application. As shown earlier, the mass fraction of burnt gun propellant z must be computed at each time step. For this purpose, z is defined by Eq.**Error! Reference source**

not found.:

$$z = 1 - \frac{m_{\text{grain}}(t)}{m_{\text{grain},0}} \tag{8}$$

or by Eq. **Error! Reference source not found.** if the cross-section of a gun propellant grain is considered constant along its own axial direction:

$$z = 1 - \frac{A_{\text{grain}}(t)l(t)}{A_{\text{grain},0}l_0} \tag{9}$$

$A_{\text{grain}}(t)$ and $A_{\text{grain},0}$ are the cross-sections at time t and t = 0 and $l(t)$ and l_0 are the lengths of a gun propellant grain at time t and t = 0. It is also important to calculate at each time step the total combustion surface $S(t)$ of a burning gun propellant grain in order to compute the evolution of its form function ϕ over time. ϕ is defined by Eq.**Error! Reference source not found.** as

$$\phi = \frac{S(t)}{S(t=0)} = \frac{2A_{\text{grain}}(t)+C_{\text{grain}}(t)l(t)}{2A_{\text{grain},0}+C_{\text{grain},0}l_0} \tag{10}$$

with $C_{\text{grain}}(t)$ and $C_{\text{grain},0}$ the circumferences of the cross-section at time t and $t = 0$. To evaluate $A_{\text{grain}}(t)$ and $C_{\text{grain}}(t)$, an image processing method has been developed. The Open-CV Python library is used in the regression routine to process images of the changing cross-section of a gun propellant grain during regression. As an example, the initial cross-section of a B7T gun propellant grain is represented by a bitmap with a black disk in Fig. 1(a) and with the 7 holes represented by white disks. For a time step dt, the gun propellant grain surface regresses of a distance $r(t) = v_c(P)\mathrm{d}t$ in the direction normal to the surface. So, at each time step, the image of the cross-section is changed to account for this regression. An example of two successive burnt thicknesses is shown in Fig. 2. The burnt thicknesses accumulate as a function of the combustion time. Therefore, the diameters $D_{\text{b}}(t)$ and $D_{\text{w}}(t)$ of the black and white disks respectively are directly linked to the burnt thickness $r(t)$ (or r_i in the discretized case) and initial diameters D_{grain} and D_{holes} through Eq. **Error! Reference source not found.**:

$$\begin{cases} D_{\text{b}}(t) = D_{\text{grain}} - 2\int_0^t r(t^*)\mathrm{d}\,t^* = D_{\text{grain}} - 2\sum_i r_i \\ D_{\text{w}}(t) = D_{\text{holes}} + 2\int_0^t r(t^*)\mathrm{d}\,t^* = D_{\text{holes}} + 2\sum_i r_i \end{cases} \tag{11}$$

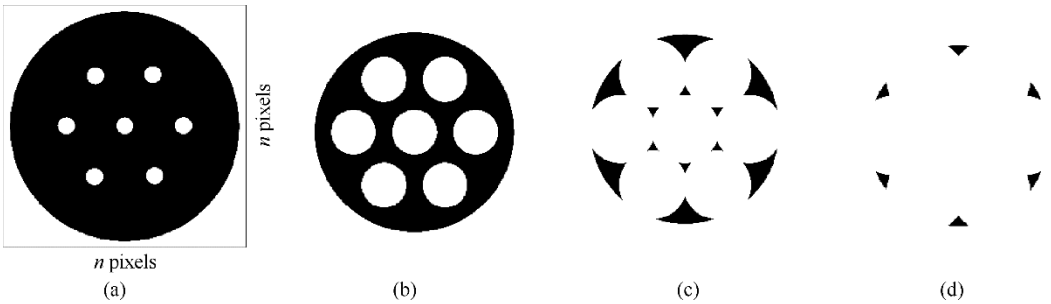

Fig. 1. Images obtained for a B7T gun propellant grain (D_{grain} = 1.143 cm and D_{holes} = 1.143 mm from Ref. [23]) with burnt thicknesses: (a) 0 mm; (b) 0.95 mm; (c) 1.4 mm; (d) 1.7 mm.

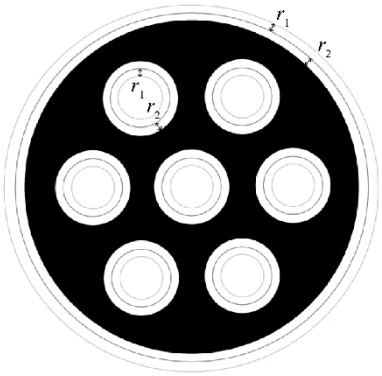

Fig. 2. Evolution of a B7T gun propellant grain cross-section with two successive burnt thicknesses.

Figs. 1(b-d) show the obtained regression history for different total burnt thicknesses. If two or more white disks meet, the resulting black slivers are generated by the imprints that the white disks leave on the central black disk as shown in Fig. 1(c).

Then, $A_{\mathrm{grain}}(t)$ is calculated by counting the number of black pixels on an image and a factor R is applied to account for the scale between the image and a real gun propellant grain. The definition of R is provided in this paper in Eq.**Error! Reference source not found.**:

$$R = \frac{D_{\mathrm{grain}}}{\mu \times n} \tag{12}$$

with μ a positive coefficient inferior but close to 1 and n the number of pixels used to describe the length of the square image of the cross-section as introduced in Fig. 1(a). The product $\mu \times n$ describes the initial size of the gun propellant cross-section in number of pixels. μ allows to create an image where the edge of an unburnt gun propellant grain is not tangent with the edge of the image in order to facilitate the detection of the gun propellant grain edges as explained later. Finally, $A_{\mathrm{grain}}(t)$ can be obtained by Eq. **Error! Reference source not found.**:

$$A_{\mathrm{grain}}(t) = R^2 n_{\mathrm{black}} \tag{13}$$

with n_{black} the number of black pixels on the image. Then, $C_{\mathrm{grain}}(t)$ is needed to calculate the lateral surface of the burning gun propellant grain. This surface is represented by the circumference of the cross-section and extends along the entire length of the gun propellant grain. To find the circumference, a function of the Open-CV library is used. This function is described in Ref. [22] and returns a list of points located on the interface between black and white areas. An example of points located at the interface and the resulting contour is shown in Figs. 3(a) and 3(b).

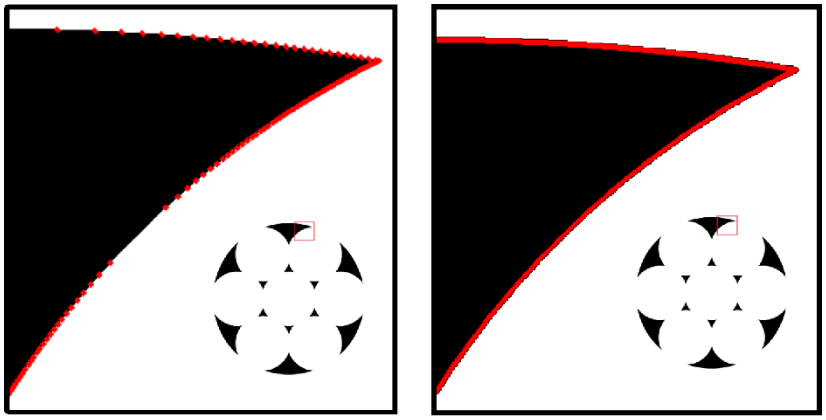

Fig. 3. Determination of a contour with (a) the location of the points of interest and (b) the resulting contour.

Finally, the circumference is the sum of all segments joining two consecutive points as shown in Eq. **Error! Reference source not found.**:

$$C_{\text{grain}}(t) = R\sum_{i=0}^{N_{\text{points}}} L_i \tag{14}$$

with N_{points} the number of points describing the interface and L_i the length of the ith segment. This method allows calculating the form function of complex perforated cylindrical gun propellant grains with very simple geometrical and mathematical tools, as well as already existing Python functions.

2.4. Performance of the gun propellant grain regression method and LPC

To validate this method, the form function of a B7T gun propellant grain is calculated and compared with the analytical form function found in Ref. [8] as shown in Fig. 4. The dimensions of the gun propellant grain come from the AGARD gun test case [23] as in Fig. 1.

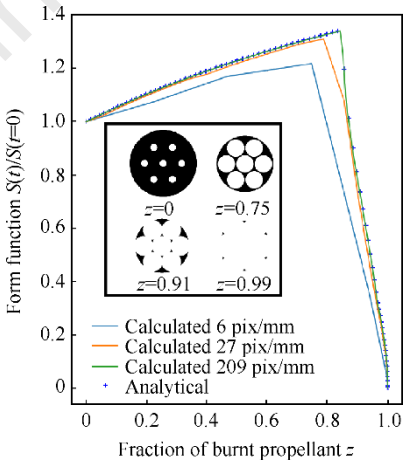

Fig. 4. Comparison between the proposed and the analytical methods for the form function calculation of a B7T gun propellant grain.

In Fig. 4, a good agreement is found with the analytical solution for images with a resolution higher than 200 pix/mm. When the regression length is smaller than the size of a pixel, the pixel remains in the image. This is a problem when the time step of the LPC is small. Pixels are only removed after several time steps, leading to crenellated regression profiles. To avoid this problem, a grayscale is considered for the pixels at the interfaces of

the black and white areas. Let's consider a pixel of size L and a regression distance r with $r < L$. The variable $\zeta = r/L$, bounded between 0 and 1, is introduced to shade the color of the interface pixels in grayscale. Since the value of white pixels is 255, the gray level of interfaces pixels corresponds to $255 \times \zeta$. In addition to accounting for small regression lengths, this technique reduces the required quality of the processed images down to 70 pix/mm to describe accurately the regression of a gun propellant grain. This minimum image resolution reduction enables the LPC code to deliver an IB profile on a gun test case in less than 25 s with Python 3.12 on an Intel Xeon CPU E5-2650 v4 2.20GHz processor. The LPC can also work with tabulated form functions for certain grain geometries. This option greatly accelerates the IB computation, with a total computational time of 0.06 s. The best of both routines is then obtained: the accuracy of the image analysis method in the regression routine and the quickness of the ballistics routine.

The regression calculation method becomes interesting for more complex perforated cylindrical geometries with multiple webs, inhibited surfaces or non-uniform hole locations. An example of different form functions for a B19T gun propellant with different kind of inhibited surfaces is shown in Fig. 5. The analytical calculation of such grains, as done in Ref.[8], would then be very complex in practice.

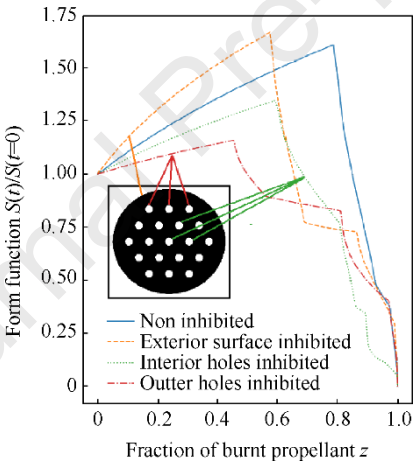

Fig. 5. Form function of a B19T gun propellant for different kind of inhibited surfaces.

The performance of the regression calculation method can be compared with the performance of Wurster's cellular automaton algorithm presented in Ref. [9]. In this method, image resolutions of 250 to 500 pix/mm are required in order to predict form functions with little error compared with analytical functions. The method presented in this article uses images with a resolution of 70 pix/mm, which presents a clear advantage in terms of data storage and calculation time. However, Wurster's method has the advantage of being able to calculate the form function of a propellant grain from a black and white photography of the initial cross-section of a real propellant grain.

3. Test cases to validate the LPC: the AGARD gun and 40 mm gun firing

3.1. Description of the test cases

In order to validate the developed LPC, the AGARD gun test case is studied. This case, introduced and described in Ref. [23], is commonly used by the ballistics community to validate their IB codes of different complexi-

ty. The results from the LPC can be compared with those of other codes from literature: IBHVG2 [24] and XKTC [25] (American 0D and 1D codes), CTA1 [26] (British 1D code by Qinetiq), Mobidic-NG [12] (French 2D axisymmetric code) and a Japanese 2D code by H. Miura and A. Matsuo presented in Ref. [27]. The characteristics of the AGARD gun case are shown in Table 1.

Table 1

Input data for the AGARD gun case.

Length of the ballistic course of the shell/mm	Adiabatic flame temperature of the igniter propellant T_{fI}/K	Gun bore diameter/mm	Impetus of the igniter propellant F_I/(MJ·kg^{-1})	Initial distance of the shell from the breech/mm	Molecular weight of the igniter combustion products/(g·mol^{-1})	Constant gun bore resistance P_{r} /MPa	Specific heat ratio of the igniter combustion products γ_{I}
4318	1706	132	0.3926	762	36.13	13.8	1.25
Shell mass,m_{shell} /kg	Gun propellant mass $m_{\mathrm{p},0}$ /kg	Mass of the propellant igniter m_I /kg	Density of the gun propellant ρ_{p}/(kg·m^{-3})	Density of the igniter propellant ρ_I /(kg·m^{-3})	Gun propellant grain geometry	Diameter of a gun propellant grain D_{grain} /mm	Adiabatic flame temperature of the gun propellant T_f /K
45.359	9.5255	0.2268	1578	1799	Cylindrical 7-holes	11.43	2585
Length of a gun propellant grain l_0/mm	Gun propellant impetus F_p /(MJ·kg^{-1})	Gun propellant grain hole diameter D_{holes}/mm	Covolume of the gun propellant combustion products b/(m^3·kg^{-1})	Gun propellant burn rate coefficient from Vieille's law α/(m·(s·MPa$^{\beta}$)$^{-1}$)	Molecular weight of the gun propellant combustion products/(g·mol^{-1})	Gun propellant burn rate pressure exponent from Vieille's law β	Specific heat ratio of the gun propellant combustion products γ_{p}
25.4	1.008	1.143	0.0010838	0.00078385	21.3	0.9	1.27

Another validation case is studied for the LPC code. It concerns an experimental 40 mm projectile. The physico-chemical properties of the propellant, the gun and the projectile are described in great detail in the work of Woodley et al. [28] and reminded here in Table 2. The results of codes such as CTA1, FHIBS, MOBIDIC or SIBIL

(0D, Ref. [29]) are also compared with the experimental case. A 440 g projectile is fired with 790 g of slotted tube propellant grain. The projectile total travel is 2.955 m for a 600 cm³ combustion chamber. The exit velocity and maximum pressure are respectively 1230 m/s and 420 MPa, and vary only slightly from shot to shot. The LPC code and the propellant grain regression method are tested on this case. The results are presented in section 3.2. . In Table 2, it can be seen that P_{r} is now described by a piecewise linear function of the distance traveled by the projectile, with decreasing pressure applied over the first centimeter of the trajectory.

Table 2

Input data for the 40 mm gun case.

Length of the ballistic course of the shell/mm	Adiabatic flame temperature of the igniter propellant T_{fI} /K	Gun bore diameter/mm	Impetus of the igniter propellant F_{I}/(MJ·kg^{-1})	Initial distance of the shell from the breech/mm	Molecular weight of the igniter combustion products/(g·mol^{-1})	Gun bore resistance P_{r} /MPa	Specific heat ratio of the igniter combustion products γ_{I}
2955	2000	40	0.287	434	57.94	14 for x < 1 cm 8 for x > 1.1 cm	1.22
Shell mass,m_{shell} /kg	Gun propellant mass $m_{\mathrm{p,0}}$ /kg	Mass of the propellant igniter m_I /kg	Density of the gun propellant ρ_{p}/(kg·m^{-3})	Density of the igniter propellant ρ_{I} /(kg·m^{-3})	Gun propellant grain geometry	Diameter of a gun propellant grain D_{grain} /mm	Adiabatic flame temperature of the gun propellant T_f /K
790	0.440	0.00415	1630	1700	Slotted tube	3.738	3416
Length of a gun propellant grain l_0/mm	Gun propellant impetus F_p /(MJ·kg^{-1})	Gun propellant grain hole diameter D_{holes}/mm	Covolume of the gun propellant combustion products b/(m³·kg^{-1})	Gun propellant burn rate coefficient from Vieille's law α/(m·(s·MPa$^{\beta}$)$^{-1}$)	Molecular weight of the gun propellant combustion products/(g·mol^{-1})	Gun propellant burn rate pressure exponent from Vieille's law β	Specific heat ratio of the gun propellant combustion products γ_{p}
400	1.1678	0.945	0.001018	0.001118	24.32	0.9718	1.2303

For both test cases, a time step of 2×10^{-6} s is used and images of 70 pix/mm are generated for the computation of the gun propellant grain regression. Decreasing the time step or increasing the image resolution from the

references does not change much the results.

3.2. Results and analysis

3.2.1. The AGARD gun test case

In order to compare the results given by the LPC with the results of codes found in literature, it is necessary to account for the duration of the gun propellant bed ignition, which is not consider in the LPC. In this study, the ignition delay Δt_{ign} obtained in a 0D code from the literature (e.g., IBHVG2) is defined as the time lapse between the simulation start of this 0D code and the moment when the breech pressure reaches the initial breech pressure used to start an LPC computation, i.e. 21 MPa. The resulting Δt_{ign} is assumed to be sufficient for the entire gun propellant bed to ignite. It takes 2 ms in the IBHVG2 result to reach a breech pressure of 21 MPa, so Δt_{ign}= 2 ms is deduced. With the $x-t$ diagram presented in Ref. [27] (2D axisymmetric code), it is possible to estimate this delay around 1.5 ms, this time by selecting the instant when the ignition front from the igniter reaches the shell base. The curves presented in Figs. 6(a) and 6(b) derived from the LPC developed in this work, are shifted by 2 ms to account for this ignition delay. Fig. 6(a) shows the time history of pressure at the breech and an additional mean pressure curve for the LPC only. Table 3 shows maximum pressures and the exit velocity at the muzzle. A good agreement is found between the LPC and the other codes when comparing these maximum values, as well as the temporal location of the pressure peak. Differences in the pressure profiles (mainly between 0D and 1D/2D codes) may be due to the difference in problem dimension, which results in pressure waves generated by localized ignition near the breech for 1D/2D codes. These waves propagate in the combustion chamber with multiple reflections at the shell base and the breech and can be seen in

Fig. *6*(b) on the pressure difference between the breech and the shell base as a function of time. For 0D codes (e.g., IBHVG2 and the LPC presented in this work), these pressure waves do not appear because the breech pressure remains most of the time higher than the base pressure according to Lagrange's assumption.

An analysis of the temporal evolution of the terms in Eq.**Error! Reference source not found.** integrated over the shell total travel at the current time is given in Fig. 7 for the AGARD gun test case. First, it can be seen that the energy balance is respected at every moment, with (U + W + Losses) equal to Q. It can also be seen that not all of the gun propellant burns, as Q does not completely reach the chemical energy of the gun propellant initial mass, as also noted by Miura and Matsuo [27], which is around 35.7 MJ for a gun propellant chemical energy of 3.7369 MJ/kg . It is reminded that the case of the AGARD gun is not really optimized and is in fact a fictitious case for validation purposes only. In fact, complete combustion of the gun propellant would be obtained for example with a heavier shell.

Table 3

Comparison of maximum pressures and muzzle velocity for different numerical approaches for the AGARD gun case.

Code	Max breech pressure /MPa	Max base pressure /MPa	Muzzle velocity /(m·s^{-1})

CEDRE + LPC (2D axi)	350	320	709
LPC (0D)	377	341	678
IBHVG2 (0D)	395	358	689
XKTC (1D)	357	330	695
CTA1 (1D)	373	343	681
MOBIDIC-NG (2D axi)	360	328	687
H. Miura, A. Matsuo (2D axi)	413	374	689

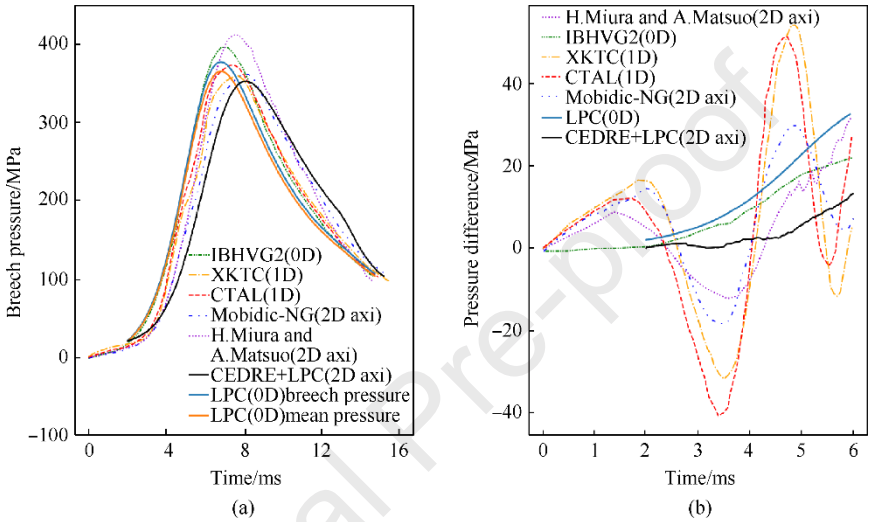

Fig. 6. (a) Breech pressure histories; (b) Pressure difference histories for the AGARD gun case.

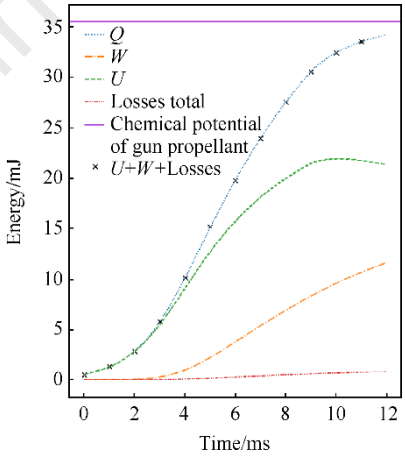

Fig. 7. Evolution of the energy terms in the energy conservation equation of IB for the AGARD gun case.

A remark can be made about the gun bore resistant pressure P_r in the AGARD case. As shown in Table 1, P_r is assumed to be constant. Nevertheless, additional tests have been carried out using a piecewise linear function, such as that adopted in Table 2 for the case of the 40 mm gun. The function consists of an initial value of 13.8 MPa applied over the first centimeter (up to 5 cm), then a linear decrease to 8 MPa over 1 mm, followed by a constant value of 8 MPa over the rest of the trajectory. The effect of this new function on the results is minimal compared to a constant P_r. A difference of around 1% is observed in the muzzle velocity or pressure profiles.

3.2.2. The 40 mm gun firing test case

As in the AGARD gun case, the LPC pressure curves for the 40 mm gun firing must be time-shifted to account for the propellant bed ignition delay. A time shift of 13.67 ms, corresponding to the average ignition delay of the experimental shots, is applied. The engraving pressure and the friction term between the projectile and the barrel are considered under a P_r function introduced in Table 2. The breech pressure curves are shown in Fig. 8 and the maximum breech and base pressures and exit velocities are given in Table 4.

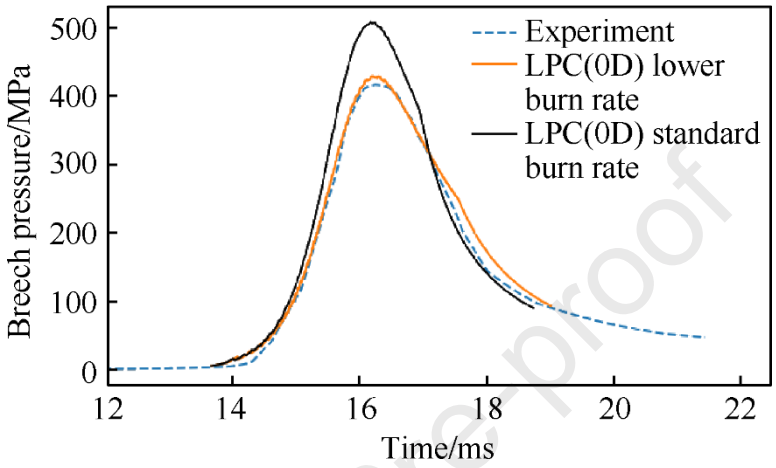

Fig. 8. Comparison of breech pressure histories between results from the LPC and the experimental shot from Ref. [28] for the 40 mm gun firing case.

Table 4

Maximum breech and base pressures and exit velocities for different codes for the 40 mm gun firing case.

Code/Experiment	Max breech pressure/MPa	Max base pressure/MPa	Exit velocity/(m·s^{-1})
Experiment	416	n/a	1229
CTA1 - standard burn rate ($\alpha = 0.1118$ cm·s^{-1}·MPa^{-n})	463	357	1244
CTA1 – lower burn rate ($\alpha = 0.107$ cm·s^{-1}·MPa^{-n})	426	329	1221
SIBIL – standard vivacity and impetus	561	439	1340
SIBIL – lower vivacity and impetus	418	327	1229
MOBIDIC-NG (tubular heating ignition)	430	382	1295
LPC - standard burn rate ($\alpha = 0.1118$ cm·s^{-1}·MPa^{-n})	516	404	1324
LPC - lower burn rate ($\alpha = 0.1018$ cm/s/MPa^{n})	428	335	1268

As with the SIBIL and CTA1 codes, the LPC results appear to be in better agreement with experimental firing data when the gun propellant is assumed to be less energetic (either by lowering the Vieille's law coefficient or its impetus). This phenomenon may be attributed to the omission of certain loss terms in the aforementioned codes, such as heat loss at the barrel walls, recoil or projectile rotation.

To briefly conclude this section, the developed LPC coupled with the regression calculation method of a gun

propellant grain makes it possible to obtain realistic physical firing conditions, such as pressure and temperature profiles and the mass flow rate of gun propellant combustion products, at low computational cost as mentioned in section 2.4. Performance of the gun propellant grain regression method and LPC.

4. Simulation of IB with a CFD code and a Dynamic Mesh Technique (DMT)

4.1. CEDRE CFD code and DMT

Once the IB LPC has been developed, the temporal profiles of the gas flow generated by the gun propellant combustion can be used in a finite volume CFD code to model the effects of IB on a moving shell. The CEDRE CFD code [30] and its CHARME solver, dedicated to complex reactive gaseous flows and developed by ONERA, are used for this study. CHARME adopts a cell-centered finite volume formalism. In this work, a second-order Monotonic Upstream Scheme for Conservation Laws (MUSCL) interpolation is used together with a Van Leer slope limiter to ensure the Total Variation Diminishing (TVD) character of the scheme. The computation of the Euler (non-viscous) fluxes is based on the HLLC scheme (a Riemann problem solver) applied to each face of the cells. The diffusive fluxes are computed with a second-order centered scheme. A first-order Euler implicit scheme is used for time integration.

CEDRE uses a DMT to compute the motion of a solid body (the shell in this study) due to the forces exerted on its walls by the surrounding fluid. Within this method, two types of meshes have to be considered, as shown in Fig. 9. A first “fixed mesh” (also called “background mesh”) is used to mesh the inside of the gun and the outside domain. A second “dynamic mesh” is used to mesh the vicinity of the moving shell as a small area of surrounding fluid. The DMT consists of two modules. A first ALE module [31] which allows CFD to be run on an arbitrary moving mesh. A second intersection mesh module to incorporate the overlapping dynamic mesh into the background mesh. At each CEDRE iteration, the forces on the shell walls are integrated and the dynamic mesh is moved accordingly. The background mesh is then intersected by the boundary of the overlapping dynamic mesh, leaving a hole imprint on the background mesh. The dynamic mesh is then inserted into this hole and the mesh connectivities are rebuilt, thus giving one unique computational mesh and preserving the conservativity of the mass, momentum and energy fluxes. This operation is performed every time step.

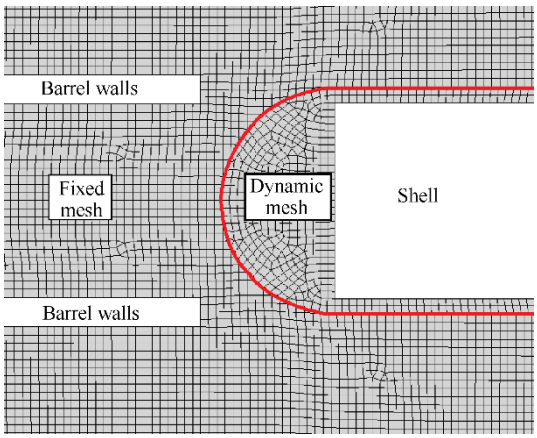

Fig. 9. Example of a configuration for the application of the DMT with a shell just leaving the gun muzzle.

4.2. Description of the test case

CEDRE is not able to properly solve the two-phase equations of IB. With the objective to further simulate BB ignition during IB and the consecutive intermediate ballistics with possible BB extinction (not presented here), some modelling elements are required to account for IB. To this end, the evolutions of the gun propellant combustion products mass flow rate, pressure and temperature produced by the gun propellant combustion calculated by the LPC are used in a CEDRE simulation as boundary conditions. Thus, the simulation is now able to faithfully reproduce the projectile motion and the physical conditions produced by IB at the projectile base. It is in this context that the AGARD gun case is reproduced once again, in order to validate the IB modelling methodology with CEDRE. The geometry of the AGARD gun is reproduced, but instead of the gun propellant initially present in the combustion chamber, a gas with uniform thermodynamic properties (same as for the gun propellant combustion products in Table 1) at the igniter adiabatic flame temperature (1706 K from Table 1) and pressure prevailing in the combustion chamber after igniter combustion (around 21 MPa) are considered. For the injection boundary conditions in CEDRE, it is stated that after several tests, they should be defined with temperature and mass flow rate profiles rather than with pressure to better preserve mass conservation between the injected mass of the gun propellant combustion products in CEDRE and the gun propellant mass used in the LPC.

CEDRE and the LPC are coupled in the following way: first, the LPC is run on the case of interest. Tables containing the instantaneous gun propellant combustion products mass flow rates from gun propellant combustion, and the average temperature of these gases are generated. A transient injection condition is then established at the walls of the gun combustion chamber (see Fig. 10) with the time-varying gun propellant combustion products mass flow rate and temperature from the LPC tables. Linear interpolation between two consecutive mass flow rates is performed by CEDRE if the LPC time step is greater than the CEDRE time step. The other boundary conditions (adiabatic walls and supersonic exit) are indicated in Fig. 10. The initial conditions for the AGARD gun case are shown in Fig. 10 and a simple cylindrical projectile is used.

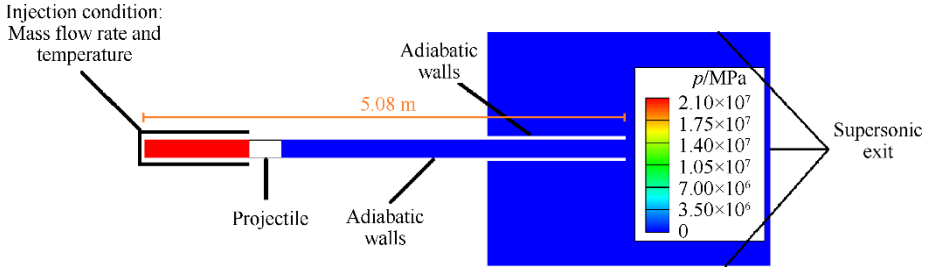

Fig. 10. Initial and boundary conditions for the AGARD gun case simulated with CEDRE.

The simulation domain is 2D-axisymetric and the Navier-Stokes equations are solved without any turbulence model. The influence of the mesh cell size on the maximum pressure in the combustion chamber is shown in Table 5. The results are similar for the medium and fine meshes. For the next simulations, a time step of 2×10^{-7} s is used with a mesh cell size of 2.75 mm. The specified mesh size corresponds to the uniform side length of the square cells between the breech and the base of the projectile on the central axis of the barrel. The mesh size at

the walls is 50 microns.

Table 5

Influence of the mesh cell size on the maximum breech pressure in the combustion chamber.

Type of Mesh	Cells size/mm	Number of cells	Max breech pressure/MPa
Coarse	11	3978	255
Medium	6.6	10892	352
Fine	2.75	62730	350

4.3. Results and analysis

The maximum pressure levels (see Table 3) and the time to reach them (see Fig. 6(a)) obtained with CEDRE and the LPC are of the same order of magnitude as for the other codes. The breech pressure profile for the "CEDRE + LPC" appears to be slightly shifted by about 1 ms compared to the "LPC" pressure profile as shown in Fig. 6(a).

There is a simple explanation for this. In CEDRE, the volume of the gun propellant grains is not taken into account. Thus, the volume left to the gun propellant combustion products (which defines its pressure) is not the one considered in the LPC until the gun propellant is completely burnt. In CEDRE, the chosen initial position of the projectile (distance of 0.762 m from the breech to the base) produces an initial volume left to the gas of 0.0104 m^3 as opposed to the volume left to the gas of 0.004 m^3 in the initial state of the AGARD case calculated with the LPC. Therefore, this volume is overestimated in CEDRE and the pressure is underestimated. This effect is particularly noticeable at the beginning of the calculation, when the gun propellant volume is not negligible compared to the combustion chamber volume. It tends to decrease when the gun propellant is close to complete combustion. To counteract this effect in CEDRE, it is possible to artificially reduce the initial volume of the combustion chamber to better account for the gun propellant volume. The corresponding breech pressure and pressure difference evolutions with a new initial volume are shown in Fig. 11. By reducing the initial chamber volume to 0.004 m^3, the pressure is now slightly overestimated in the calculation because the reduction in gun propellant volume (0.0064 m^3) and the conversion in the gun propellant combustion products due to combustion are not considered.

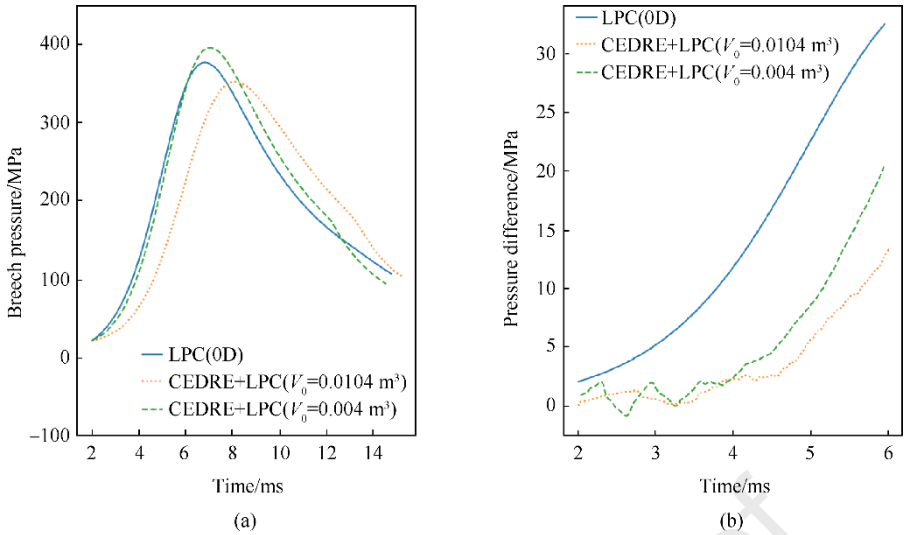

Fig. 11. Pressure for different initial chamber volumes: (a) Breech pressure; (b) Pressure difference evolutions.

Even though the breech pressure seems to be slightly overestimated compared to the LPC alone, an initial chamber volume of V_0= 0.004 m³ seems to give good results and significantly reduces the time delay of the pressure peak as shown in Fig. 11(a). A muzzle velocity of 693 m/s is obtained with V_0= 0.004 m³, which is also closer to the literature results in Table 3 and demonstrates the capacity of the CEDRE+LPC method to reproduce IB conditions.

5. Muzzle flow simulation during intermediate ballistics

Now that the IB simulation has been validated with CEDRE, it is interesting to extend the calculation to demonstrate that CEDRE can also calculate intermediate ballistics in reacting conditions. To this end, the simulation case presented by Zhuo et al. [13] is studied with the same shell geometry. The shell, that is equipped with a BB unit, is initially placed at the muzzle of the gun. The 130 mm gun is initially loaded with a gas at 60 MPa and 2500 K and with a muzzle velocity of 900 m/s along the gun axis. The gun propellant combustion products initially present in the gun are composed of several species whose mass fractions are given in Table 6. The rest of the domain is air at rest (300 K, 1.01325 bar).

Table 6

Composition and mass fractions of the gun propellant combustion products from Ref.[13].

CO	H_2	CO_2	H_2O	N_2
0.5138	0.0157	0.2153	0.1293	0.1259

In section 5, the general settings of CEDRE remain the same as those described in section 4.1. In a first step (see section 5.1), intermediate ballistics is directly simulated with the initial conditions of Ref.[13] with CEDRE in order to validate the intermediate ballistics simulation. In a second step (see section 5.3), intermediate ballistics is simulated directly after IB. The aim is to recover the same muzzle conditions (base pressure and muzzle velocity of the shell) as in Ref. [13] when the shell exits the gun. For this purpose, an inverse problem is introduced and

solved in section 5.2. Knowing the characteristics of the gun, an algorithm is developed to find the gun propellant characteristics (mass, impetus and grain dimensions) to obtain the desired muzzle velocity and shell base pressure at the muzzle.

5.1. Direct simulation of intermediate ballistics without diffusion effects

In this section, an intermediate ballistics simulation under the same main conditions as Ref. [13] is carried out in order to validate the simulation of this isolated phase. In particular, the shell velocity is initially set to 900 m/s and remains constant throughout the simulation. The boundary condition at the breech of the gun is specified as a supersonic inlet (900 m/s, 60 MPa and 2500 K) to be in agreement with the state of the gas initially present in the gun. This contradicts Lagrange's assumption of zero gas velocity at the breech but this choice of boundary condition has no impact on the first instants of the intermediate ballistics. The other walls of the gun and the shell are adiabatic walls and the domain exits are considered supersonic. An Euler reactive multispecies simulation is carried out with CEDRE as done in Ref. [13]. The chemical kinetics used to account for the combustion of the gun propellant combustion products, whose composition is given in Table 6, is the same as in Ref. [13] and comes from Ref. [32].

Simulations are performed with different mesh resolutions. The coarse, medium and fine meshes consist of 3×10^5, 7×10^5 and 1.2×10^6 cells for the fixed mesh, and 3×10^3, 5×10^3 and 9×10^3 cells for the dynamic mesh, respectively. For comparison purposes, the mesh used in Ref. [13] is composed of 10^6 cells but a mesh of 7×10^5 cells gives the same results on the temperature profile according to Ref. [13]. A visualization of the medium mesh is shown in Fig. 12. The mesh characteristic cell sizes in the different refinement regions are summarized in Table 7. The influence of the cell sizes in regions B, C and D on the temperature profile between the muzzle exit plane and the shell base on the symmetry axis at t = 1 ms is studied with the results shown in Fig. 13. The mesh is not refined in a specific zone but in the entire domain of interest.

Table 7

Cell sizes of the medium mesh for the intermediate ballistics simulation.

Region	A	B	C	D
Cell size /mm	6.5	2	1.7	0.5

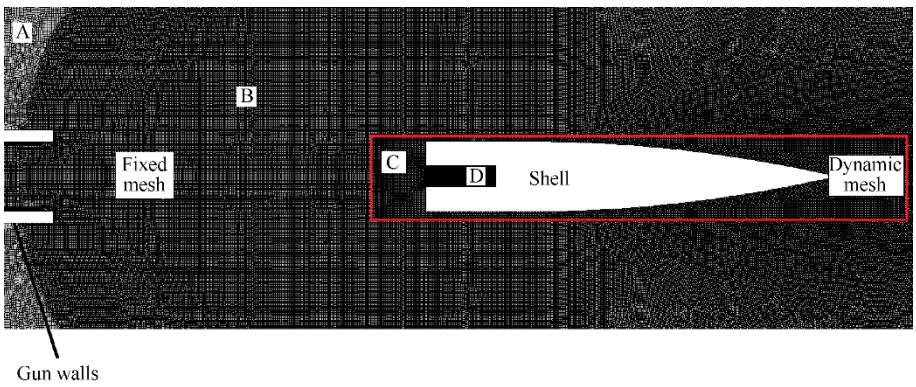

Fig. 12. Visualization of the medium mesh for intermediate ballistics simulation.

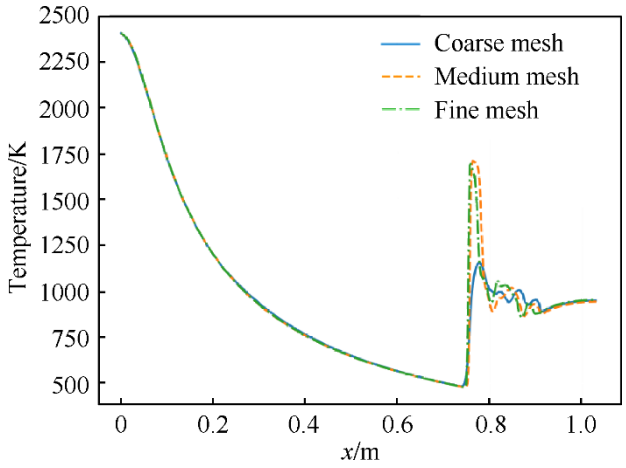

Fig. 13. Temperature profiles along the symmetry axis between the muzzle exit plane and the shell base at t= 1 ms for different mesh resolutions.

The simulation is performed with the medium mesh as the lower cell sizes of the fine mesh do not provide a significant improvement. Time integration is performed with a first-order implicit method with a time step of 2×10^{-7} s. Table 8 shows the computational cost of simulating intermediate ballistics on the medium mesh. With a total number of 7×10^{5} cells for the medium mesh, the number of CPU cores was set at 96, giving a number of cells per CPU core of around 7200. This choice was motivated by the fact that CEDRE has a good scalability for a number of cells per CPU core remaining above 7000.

Table 8

Medium mesh computational cost for intermediate ballistics only.

Number of CPU cores	Total CPU time/s	Mean CPU time per iteration/s
96	3.2×10^{6}	125.1

Mach number and temperature fields are compared at t = 0.2 ms, t = 0.5 ms and t = 1.5 ms with Ref. [13] in Figs. 14 and 15. In both Figs, the Mach and temperature field values and their structures are very similar at t = 0.2 ms. For the other instants, the CEDRE fields show more and more perturbations, but nevertheless present a very similar overall structure and field values are still close to Ref. [13].

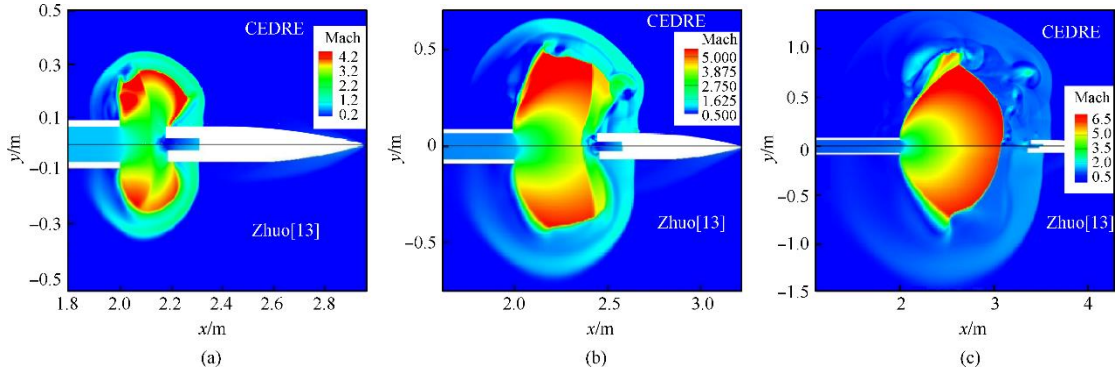

Fig. 14. Comparison of the Mach number fields between CEDRE and Ref.[13] at (a) t = 0.2 ms, (b) t = 0.5 ms and (c) t = 1.5 ms.

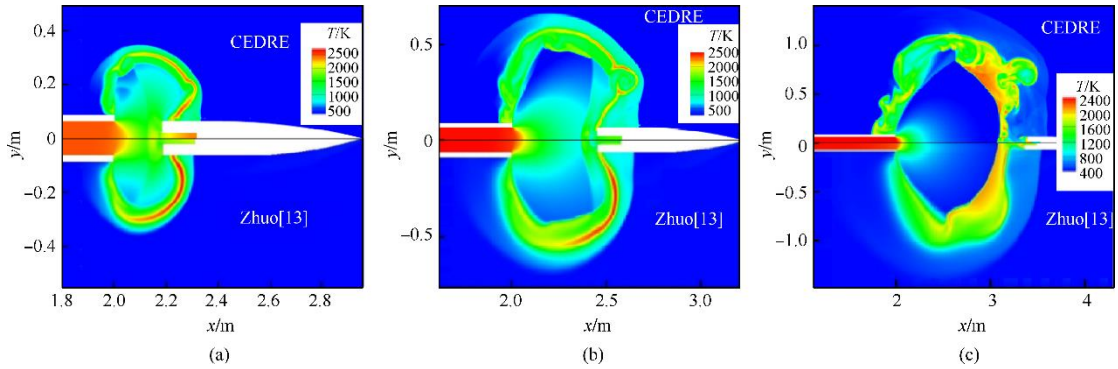

Fig. 15. Comparison of temperature fields between CEDRE and Ref.[13] at (a) t = 0.2 ms, (b) t = 0.5 ms and (c) t = 1.5 ms.

Given the overall similarity of the Mach number and temperature fields between CEDRE and Ref.[13], it can be concluded that CEDRE is capable of simulating intermediate ballistics. The remaining differences can be due to different meshing strategies and numerical methods. Nevertheless, the same shockwave structure and flame front are obtained. A more detailed analysis of the flow structure and flame front is presented later in section 5.3.

5.2. Inverse problem to find an optimal gun propellant configuration for IB

In this section, a gun propellant configuration is searched in order to recover the initial muzzle conditions of Ref.[13]. The geometric characteristics of the gun are fixed (a length of 6 m and a caliber of 130 mm). The shell weight is not given, so a mass of 30 kg is assumed. This shell mass makes it possible to find realistic gun propellant configurations with the gun geometry presented in Ref. [13]. In this study, a gun propellant configuration is defined by a set of three parameters in a 3D space: total mass, impetus and grain length (a B7T grain defined by $D_{grain,0}$ = 11.43 mm and D_{holes} = 1.143 mm). For a given gun propellant mass, the grain length defines the total number of grains and therefore the burning surface. All other parameters are kept identical to those of the AGARD gun case. To map the different possible configurations in the 3D space, a Latin hypercube sampling method is adopted. This statistical method is used to generate a near-random sample of parameter values from the defined 3D space. It ensures that each sample remains the only one in each axis-aligned hyperplane containing it. In other words, no generated gun propellant configuration can have parameters in common with any other configuration. In particular, this method makes it possible to sample in every variation interval of the parameters with a uniform probability. The variation intervals of the three parameters are shown in Table 9. The ranges of variation of the gun propellant mass and the length of the grains correspond to conventional artillery values. The range of variation of the impetus is adjusted to obtain realistic solutions from the LPC and avoid numerical errors.

Table 9

Variation intervals for B7T gun propellant parameters.

	Minimum	Maximum
X: gun propellant total mass $m_{p,0}$ /kg	10	13
Y: gun propellant impetus F_p /MJ·kg^{-1}	0.4	0.9

Z: gun propellant grain length l_0 /mm	18.5	23

Each sample is then tested in the LPC, and only those leading to a muzzle velocity of 900 m/s and a muzzle base pressure of 60 MPa (with a margin of error of 1%) are retained. Then, the selected configurations can be represented in the parameters space under a 3D curve, as shown in Fig. 16. On these graphs, the parameters space of tested configurations is represented by a cube, with the blue and red faces representing examples of physical limits for the minimum grain length and maximum gun propellant mass respectively. Below the blue face, for grain lengths less than 18.5 mm, the larger combustion surface associated with a higher number of grains leads to an excessive pressure and an error output in the LPC. A similar error is obtained for gun propellant masses higher than 13 kg, above the red face of the cube.

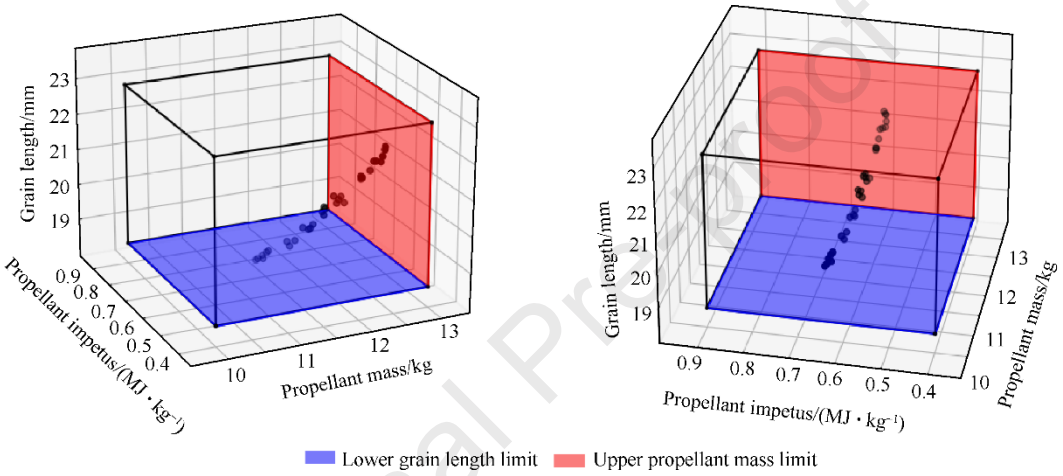

Fig. 16. Gun propellant parameters giving valid muzzle velocity and base pressure at 1% with case [13].

In the parameters space, the straight line minimizing the deviation from these points has a directing vector expressed by Eq.**Error! Reference source not found.**:

$$\vec{n} = \begin{pmatrix} a \\ b \\ c \end{pmatrix} = \begin{pmatrix} 4.85 \\ -0.23 \\ 8.74 \end{pmatrix} \tag{15}$$

Gun propellant configurations that meet the requirements of Ref. [13] within 1% error verify Eq.**Error! Reference source not found.** for q values in [0,0.32]:

$$\begin{cases} X = X_0 + q.a = 11.45 + 4.85q \\ Y = Y_0 + q.b = 0.673 - 0.23q \\ Z = Z_0 + q.c = 18.55 + 8.74q \end{cases} \tag{16}$$

with (X_0, Y_0, Z_0) representing a point near the lower limit of the grain length, which verifies the required gun performance of case [13]. The upper limit of the q variation range ensures that the maximum gun propellant mass of 13 kg is not exceeded.

A parametric study is carried out on some of the LPC input parameters to gain a better understanding of possible variations in results. First, a B19T propellant with the same grain diameter and perforation diameter as a B7T propellant is considered and compared with the results previously obtained in Fig. 16 for the B7T propellant. As shown in Fig. 17(a), the lower limit for the B19T propellant in grain length is 29 mm and the upper limit in

propellant total mass is 11.7 kg. The variation intervals of the three parameters with a B19T gun propellant grain are shown in Table 10.

Table 10

Variation intervals for B19T gun propellant parameters.

	Minimum	Maximum
X: gun propellant total mass $m_{p,0}$ /kg	8	11.7
Y: gun propellant impetus F_p /MJ·kg^{-1}	0.4	1.05
Z: gun propellant grain length l_0 /mm	29	50

The propellant impetus to achieve the desired muzzle conditions is similar to that of conventional artillery, i.e. approximately 1 MJ/kg for short grain lengths and low total propellant mass as shown in Fig. 17(a). The impetus found for B7T propellant grain did not exceed 0.7 MJ/kg, which is quite low for an artillery propellant. The comparison between the B7T and B19T acceptable ranges of parameters is illustrated in Fig. 17(a). A second parametric study is performed on the shell mass effect, with the same variation intervals and B19T grain geometry. A modification of ±2 kg in the shell mass is applied and the resulting acceptable configurations are illustrated in Fig. 17(b).

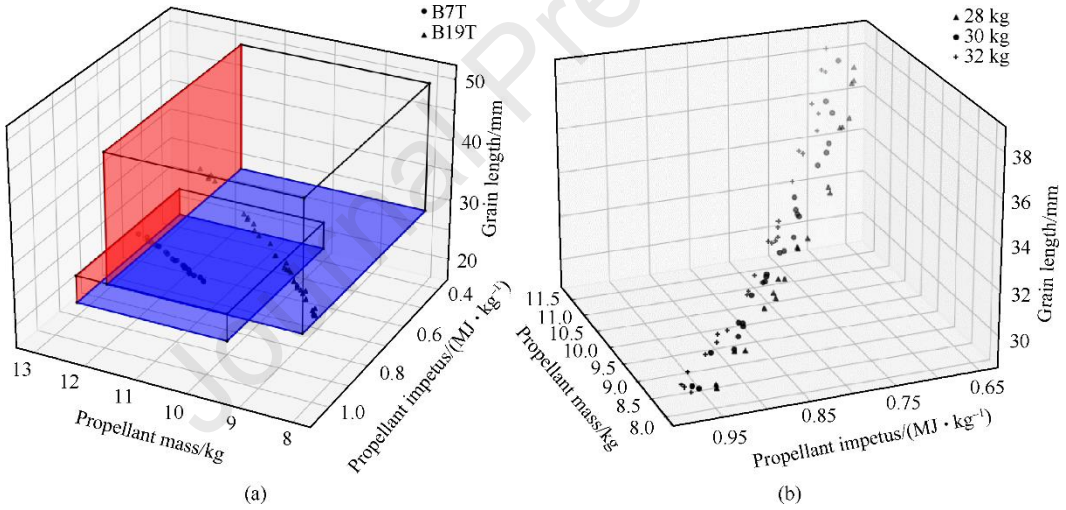

Fig. 17. Comparison of gun propellant parameters giving valid muzzle velocity and base pressure at 1% with case [13] for (a) a B7T and B19T propellant grain and (b) for different shell mass with a B19T propellant grain.

5.3. IB and intermediate ballistics simulation with diffusion effects

The latter gun propellant configuration (X_0, Y_0, Z_0) is chosen in order to simulate IB with the CEDRE+LPC methodology and with the geometry presented in Ref. [13]. The mesh refinement is the same as in section 5.1 (medium mesh). Using the injection method described in section 4.1 and Fig. 10 for the unsteady boundary conditions, CEDRE+LPC gives the same muzzle conditions as those used in Ref.[13] (60 MPa and 900 m/s). In this section, the Navier-Stokes equations are solved with the $k-\omega$ SST turbulence model presented in more details in Ref. [33], in contrast with section 5.1 (Euler equations), with the same mesh and time step. For the complete simulation of IB and intermediate ballistics, the computational cost is indicated in Table 11.

Table 11

Medium mesh calculation performances for IB and intermediate ballistics.

Number of CPU cores	Total CPU time/s	Mean CPU time per iteration/s
96	12.2×10^6	130

During the shell acceleration phase, the compression waves at the nose of the shell merge to form a precursor shock (see (1) in Figs. 18(a) and 18(b)). This wave structure is similar to that generated by the movement of an accelerating piston. The shock eventually exits the gun, is diffracted and becomes spherical (see (1) in Figs. 18(c) and 18(d)). Next comes a phase in which the pressurized air set in motion by the shell escapes the gun and undergoes a Prandtl-Meyer expansion. A typical structure of an under-expanded jet is then visible at the gun muzzle (see (3) in Figs. 18(c) and 18(d)). This structure is described in greater depth below. This part of the flow was not visible in the simulations of Ref. [13], as the shell acceleration phase was not simulated.

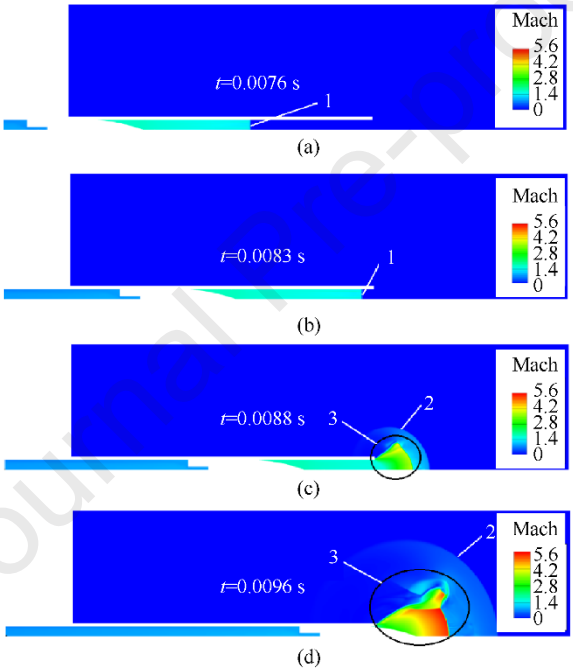

Fig. 18. Mach number fields of the air flow revealing the precursor shock exiting the gun and the formation of the Prandtl-Meyer expansion.

The temperature fields at the muzzle when the shell exits the barrel are shown on the upper half in Fig. 19 for IB and intermediate ballistics calculated successively. Results of intermediate ballistics alone with the Navier-Stokes equations and $k-\omega$ SST turbulence model are shown on the lower half in Fig. 21 for comparison purpose. In this simulation, the muzzle conditions are the same as for Ref. [13] (60 MPa, 2500 K and 900 m/s). The precursor flow and the flow resulting from the expansion of the gun propellant combustion products behind the shell have the same structure and can therefore be described in the same way (the precursor flow being less under-expanded but presenting similarities with the expansion of the gun propellant combustion products). Expansion waves reflect off the surface of the jet in a compression wave beam. This beam focuses to form a shock visible in Fig. 19(c) (see (1)). A Mach disk (2) and a reflected shock (3) can also be seen developing from a triple point. The

precursor shock previously formed can still be seen at t = 1.5 ms (see (4) in Fig. 19(c)). The gases expanding at high velocity from the muzzle hit a stagnation point on the shell base and a shock is formed just before (see (5) in Figs. 19(a) and 19(b)). Finally, a spherical shockwave (6) expanding radially can be seen.

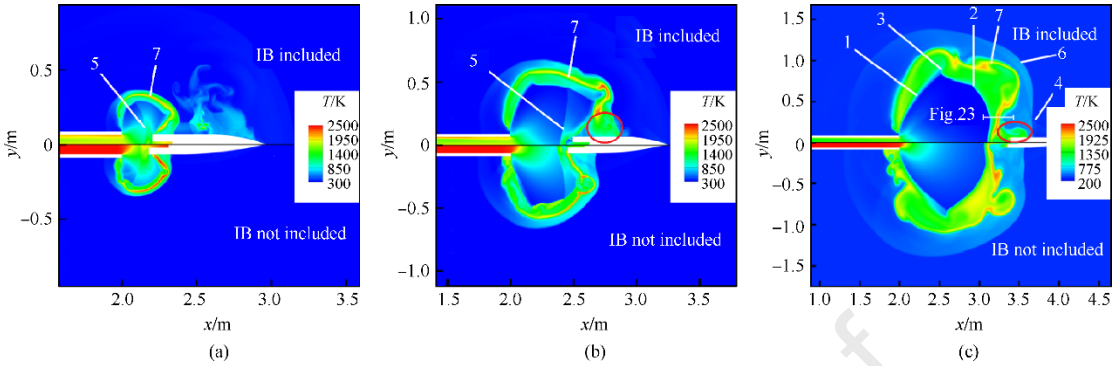

Fig. 19. Comparison of temperature fields with and without IB simulation at (a) t = 0.2 ms, (b) t = 0.5 ms and (c) t = 1.5 ms.

Due to the presence of high-pressure propellant gases in the central channel of the base bleed, an under-expanded jet structure at the BB outlet can also be observed. The strong depressurization generated by the exit of these gases from the BB can possibly lead to transient combustion or even BB extinction (not accounted here). The depressurization levels in the central channel of the BB for different muzzle pressures as a function of time are plotted in Fig. 20. Time variations in pressure are calculated at various points along the central axis of the BB channel. These pressure variations are averaged and compared with the results of Ref. [13]. A depressurization peak, which in some cases can be well over of 100 MPa/ms, is observed at around 0.16 ms.

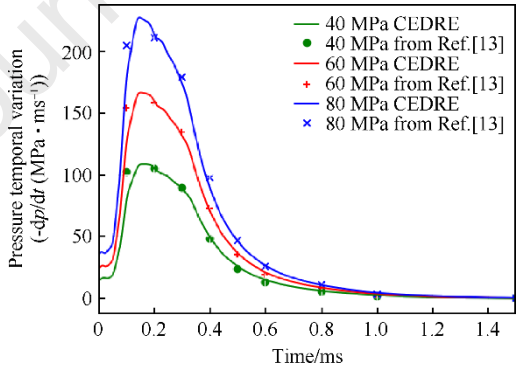

Fig. 20. Evolution of the temporal gradient of the BB mean pressure for different initial pressures.

Comparing simulations with and without IB (upper and lower half of Fig. 19), it appears that the flow structure is similar, and the precursor shock and related flow do not show any significant effect on the main gun propellant combustion products expansion. However, there is a difference in the area circled in red in Figs. 19(b) and 19(c). This difference comes from the blast wave (generated by the gun propellant combustion products expansion) encountering air from the precursor flow which is not at rest, unlike in the “IB not included” case. As in Fig. 15, a high-temperature arc (7) appears after the Mach disk. This arc corresponds to the zone where the gun propellant combustion products react with the oxygen present in the air. As mentioned by Klingenberg and Mach

[34], this zone is called intermediate flash and features a high-intensity flash of light. The Heat Release Rate (HRR in W/m³) for both cases visible in Fig. 21 confirms this observation (see (2)). The fact that the reaction zone appears after the Mach disk is due to the temperature increase of the gun propellant combustion products as they pass the Mach disk. It is also in this zone that mixing between the reacting species and oxygen is possible as mentioned in Ref. [34]. What is new compared to the results in Fig. 15 is that the gun muzzle temperature of 2500 K chosen from Ref. [13] is quite different from the one generated by the IB cycle calculated with CEDRE, which is only 1800 K. Indeed, the solving method for the inverse problem only accounts for the muzzle velocity and base pressure and not for temperature. Moreover, a temperature of 2500 K for the gun propellant combustion products at the gun muzzle might not be realistic with a muzzle velocity of 900 m/s and a base pressure of 60 MPa. For instance, in Ref. [15] and Ref. [35], a smaller projectile is set in motion and reaches a muzzle velocity of about 900 m/s at a pressure of 50 MPa and a temperature of 1800 K, similar to the temperature found with the "IB included" in Fig. *19*.

Finally, a conical zone at the muzzle (see (a) in Fig. 21) with a non-zero HRR is also noticed. This conical zone is located where the primary flash usually appears as evoked in Ref. [34]. Nevertheless, it is difficult to say whether the high HRR observed in that zone actually corresponds to the primary flash. Usually, the primary flash is caused by thermal excitation of the particles (soot or solid reaction products) or potassium and sodium-based additives present in the gun propellant combustion products, which are not considered in these calculations. Here, the cause of the high HRR seems to come solely from a change in the composition of the gun propellant combustion products at the muzzle.

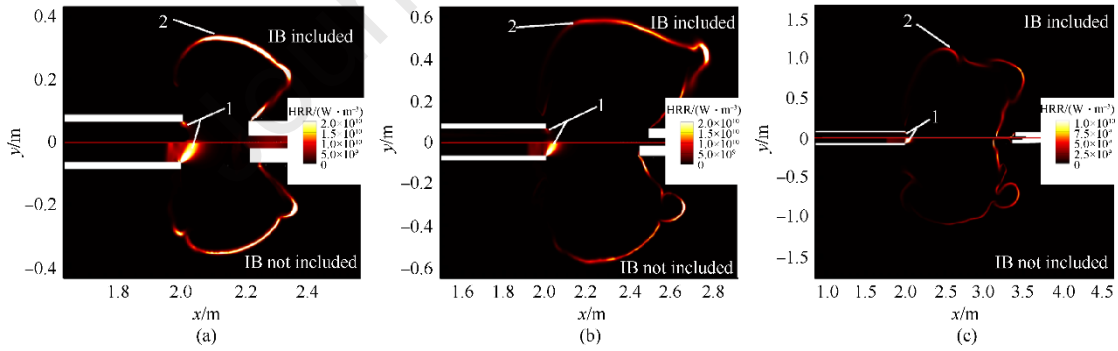

Fig. 21. Comparison of heat release rate fields with and without IB simulation at (a) t = 0.2 ms, (b) t = 0.5 ms and (c) t = 1.5 ms.

HRR and gun propellant combustion products consumption and production through zone (a) in Fig. 21 are plotted in Fig. 22. This high HRR zone is located at the expansion fan of the muzzle flow. The only difference between the two figures is whether or not IB is included. Then, the main difference is the temperature of the gun propellant combustion products at the gun outlet (1800 K for Fig. 22(a), 2500K for Fig. 22(b)). Consumption or production of a species k is defined by the ratio $\left(Y_k(x) - Y_k(x = -\infty)\right)/Y_k(x = -\infty)$, which is positive (resp. negative) for production (resp. for consumption). A peak in HRR is noticed in Fig. 22(b) for a temperature of 2500

K. Recombination of the species present in the gun propellant combustion products is observed. CO and H_2O are consumed whereas H_2 and CO_2 are produced. For instance, reactions presented in Eqs.**Error! Reference source not found.**) and **Error! Reference source not found.**) (with activation energies of -3.1 kJ/mol and -19 kJ/mol respectively) from the chemical kinetics appear to be responsible for the CO_2 production and CO consumption.

$$\mathrm{CO} + \mathrm{OH} \leftrightarrow \mathrm{CO_2} + \mathrm{H} \quad (17)$$

$$\mathrm{CO} + \mathrm{O} + \mathrm{M} \leftrightarrow \mathrm{CO_2} + \mathrm{M} \quad (18)$$

Both reactions have negative activation energies and are therefore strongly favored when temperature drops in the expansion fan at the gun muzzle. Such negative values may not be usual in chemical kinetics but can be found in other reaction schemes. A more detailed reaction scheme described by Westbrook [36] containing 12 species (CO, CO_2, HCO, H, OH H_2O, H_2O_2, HO_2, H_2, O_2, N_2 and O) and 28 reactions is also tested. The temperature field in the intermediate flash does not vary when compared with previous simulations, and the zone at the exit of the gun with a non-zero HRR is still present with the same HRR values. In fact, this reaction scheme also contains the CO_2-generating reaction ($CO + OH \leftrightarrow CO_2 + H$) with negative activation energy (E_a = -3.2 kJ/mol). In this reaction scheme, the second reaction ($CO + O + M \leftrightarrow CO_2 + M$) has a positive activation energy (E_a= 17.2 kJ/mol) but this difference does not seem to affect the results. The HRR peak is explained by the production of final species, such as CO_2, with high enthalpy of formation ($\Delta_f H°_{CO_2}$= -393.5 kJ/mol). No noticeable change in temperature is observed at the HRR peak for both cases and both reaction schemes because of the severe depressurization of the gun propellant combustion products. These differences in the description of reaction schemes suggest a future parametric study on the influence of the kinetics during intermediate ballistics.

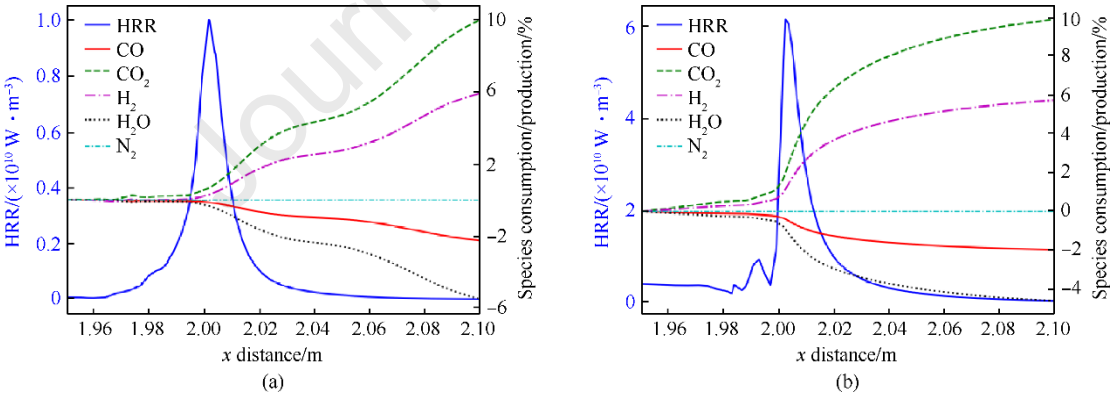

Fig. 22. Heat release rate and species consumption / production in the primary flash with (a) IB included and (b) IB not included.

The mass fractions of various species and temperature are plotted across the Mach disk and flame front in Fig. 23 from the white line shown in Fig. 19(c). Temperature rises drastically as the Mach disk is crossed (ignition point is reached) which, together with the presence of O_2 after the Mach disk, make chemical reactions possible as mentioned before. The reaction zone appears at the contact surface between the gun propellant combustion products and the ambient air (containing O_2) as is usually the case for a diffusion flame. The CO_2 mass fraction increases around x = 3.17 m where the flame front is located. In fact, at this position, CO and H_2 oxidize with O_2 to

form CO_2 and H_2O. The increase in H_2O is not visible because the amount of H_2 is quite small compared to CO. The position of the flame front is also confirmed by the maximum of the OH radical mass fraction and temperature at x = 3.24 m. As explained by Poinsot et al. [37], diffusion flames cannot propagate on either the fuel or oxidizer sides (too rich on one side, too lean on the other). The flame remains therefore localized at a precise coordinate, making it quite sensitive to velocity fluctuations and hence to turbulence. Since the flow after the Mach disk is actually turbulent (k = 10^4 - 10^5 m²/s²), one perspective of this work would be to consider the interaction between turbulence and combustion in this zone.

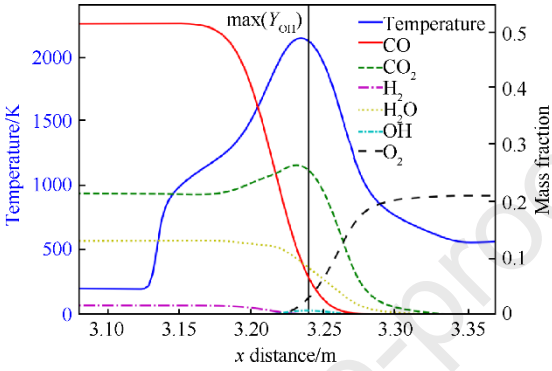

Fig. 23. Temperature and mass fractions of different species through the Mach disk and flame front from the white line in Fig. 19(c).

6. Conclusions

The results of this paper were obtained with a methodology accounting for multiple numerical tools coupled together in the context of large caliber launch dynamics: an LPC to compute IB, an original image processing method to calculate gun propellant grains regression, an inverse method to solve for an IB related inverse problem, a DMT ensuring mass, momentum and energy conservativity and a CFD reactive code.

In particular, the LPC code is validated thanks to the AGARD gun case and a 40 mm gun case and shows good results when compared to the results of similar codes available in literature. Coupled with the CEDRE CFD code and a DMT, it is possible to model IB with CEDRE, which is unable to properly simulate IB at this stage. Once again, this method is validated with the AGARD case and demonstrates good results.

A simulation of intermediate ballistics alone without diffusion effects is then carried out with CEDRE and validated against the work of Ref. [13]. A gun propellant configuration giving the muzzle conditions of Ref. [13] is found using a Latin hypercube sampling method. A successive IB and intermediate ballistics simulation is finally carried out with diffusion effects, enabling the flame front, precursor shock and gun propellant combustion products depressurization in a BB channel to be studied. The gun muzzle flow and BB depressurization levels correspond to the results found in literature, which validate the numerical methodology. Some insights of various reactive fronts related to primary and intermediate flashs locations were presented. A diffusion flame regime producing CO_2 is obtained when CO at high temperature (after passing though the Mach disk) meet O_2 in the air.

Production of CO_2 is also obtained in the gun propellant combustion products muzzle expansion without O_2, due to particular Arrhenius coefficients.

The first applications of the developed methodology demonstrate very good agreements with state-of-the-art results. These first steps were essential to go further on the study of a BB operation in IB and intermediate ballistics. Perspectives first concern the study of BB ignition during IB due to convective heat transfers from the gun propellant combustion products. An ignition model will be applied to determine the ignition delay of the BB and its mass consumption before exiting the gun muzzle. Second, after being ignited in IB, the BB can be subjected to extinction due to the strong depressurization produced by the muzzle flow during intermediate ballistics. In order to account for that risk, a specific transitory combustion model for solid propellant will be implemented in CEDRE and tested.

References

[1] Carlucci, D. E. Ballistics: Theory and Design of Guns and Ammunition (1st ed.). CRC Press. 2007. https://doi.org/10.1201/9781420066197

[2] Oswatitsch, K. Intermediate Ballistics. In: Schneider, W., Platzer, M. (eds) Contributions to the Development of Gasdynamics. Vieweg+Teubner Verlag, pp 343-372. 1980. https://doi.org/10.1007/978-3-322-91082-0_21

[3] Ye, R., Yu, Y., & Cao, Y. Experimental study of transient combustion characteristics of AP/HTPB base bleed propellant under rapid pressure drop. *Combustion Science and Technology*, *187*(3), 445–457. 2015. https://doi.org/10.1080/00102202.2014.951121

[4] Gaillard, T., Devillers, R. W., Demarthon, R., Heddadj, S., Le Boursicaud, H., Lestrade, J.-Y., Schwartz, J.-S., Grignon, C., Teyssier, N., & Fougeroux, P. *Experimental and numerical methodologies to characterize base bleed operation in internal ballistics conditions. EUROPYRO 2023*

[5] Lecoustre, M., Gauchoux, J., & Coupez, D. Base Bleed Solid Propellant*.* Proceeding of the First International Symposium on Special Topics in Chemical Propulsion: Base Bleed. Greece, 1988

[6] Xue, X., Yu, Y., Yu, W., & Zhang, Q. (2017). Numerical studies on chemical non-equilibrium flow of the base-bleed unit wake. *Combustion Science and Technology*, *189*(8), 1416–1439. 2017. https://doi.org/10.1080/00102202.2017.1305365

[7] Ongaro, F., Robbe, C., Papy, A., Stirbu, B., & Chabotier, A. Modelling of internal ballistics of gun systems: A review. In Defence Technology. KeAi Communications Co, 2024. https://doi.org/10.1016/j.dt.2024.05.004

[8] Stals, J. Form-Functions for Multi-Component Propellant Charges Including Inhibited Grains and Slivers Burns. Materials Research Laboratories, Maribyrnong, Victoria, Australia, MRL-TN-371, 1975

[9] Wurster, S. Modeling, Simulation and Characterization of Complex Shaped Solid Propellant Combustion. Propellants, Explosives, Pyrotechnics, 42(7), 736–748, 2017. https://doi.org/10.1002/prep.201700078

[10] Wang, J., Xiong, Y., & He, X. Simulation of Solid Propellant Regression with Cracks Based on Level-Set Method. Journal of Physics: Conference Series, 2478(3), 2023. https://doi.org/10.1088/1742-6596/2478/3/032029

[11] Guerrero, J. Numerical simulation of the unsteady aerodynamics of flapping flight. University of Genoa, Italy, 2009. http://linkinghub.elsevier.com/retrieve/pii/089543569090155I

[12] Della Pieta, P., & Reynaud, C. Numerical Investigations for Modeling Interior Ballistics Two-Phase Flow. SNPE-CRB, B.P. n°2. Vert Le Petit, France. 137–148

[13] Zhuo, C., Feng, F., Wu, X., Liu, Q., & Ma, H. Numerical simulation of the muzzle flows with base bleed projectile based on dynamic overlapped grids. Computers & Fluids, 105, 307-320, 2014. https://doi.org/10.1016/j.compfluid.2014.08.006

[14] Zhang, H., Chen, Z., Jiang, X., & Li, H. Investigations on the exterior flow field and the efficiency of the muzzle brake. Journal of Mechanical Science and Technology, 27(1), 95–101, 2013. https://doi.org/10.1007/s12206-012-1223-8

[15] Qin, Q., & Zhang, X. Numerical investigation on combustion in muzzle flows using an inert gas labeling method. International Journal of Heat and Mass Transfer, 101, 91–103, 2016. https://doi.org/10.1016/j.ijheatmasstransfer.2016.05.009

[16] Cayzac, R., Carette, E., Alziary De Roquefort, T., Renard, F. X., Roux, D., Balbo, P., & Patry, J. N. Computational fluid dynamics and experimental validations of the direct coupling between interior, intermediate and exterior ballistics using the Euler equations. Journal of Applied Mechanics, Transactions ASME, 78(6), 2011. https://doi.org/10.1115/1.4003812.

[17] Berthelot, M. Sur la force des matières explosives d'après la thermochimie (Vol. 2). Gauthier-Villars, 1883.

[18] Gaunce, M. T., Osborn, J. R. (1986). Temperature sensitivity coefficients of solid propellant burning rate. Acta Astronautica, 13(3), 127–130. https://doi.org/10.1016/0094-5765(86)90044-5

[19] Baer, P. G., & Frankle, J. M. The Simulation of Interior Ballistic Performance of Guns By Digital Computer Program Aberdeen Proving Ground, Maryland, 1962

[20] STANAG 4367 (unclassified) Ed. 3. Thermodynamic Interior Ballistics Model with Global Parameters. Mas/0588-Land/4367, 4367(Edition 2), 2000

[21] Morrison, W. F., Wren, G. P., Oberle, W. F., and Richardson, S. L. The application of Lagrange and Pidduck-Kent gradient models to guns using low molecular weight gases. Technical report, U.S. Army Research Laboratory, 1993. https://apps.dtic.mil/sti/pdfs/ADA261768.pdf

[22] Suzuki, S., & be, K. A. Topological structural analysis of digitized binary images by border following. Computer Vision, Graphics and Image Processing, 30(1), 32–46, 1985. https://doi.org/10.1016/0734-189X(85)90016-7

[23] Work Group No. 5, Fluid Dynamics Aspects of Internal Ballistics. AGARD Advisory Report No. 172, NATO, 1982

[24] Anderson, R. D., & Fickie, K. D. IBHVG2 – A User's Guide. US Army Research Laboratory, Aberdeen Proving Ground, Maryland, BRL-TR-2829, 1987

[25] Gough, P. S. The XNOVAKTC code. Technical report. Ballistic Research Laboratory Aberdeen Proving Ground, Maryland, 1990

[26] Woodley, C., Critchley, R., Wallington, D., & Tn, K. QinetiQ Studies on Wear and Erosion in Gun Barrels. The Control and Reduction of Wear in Military Platforms, Williamsburg, USA, 7-9 June, June, 15–1 to 15–12, 2003. https://apps.dtic.mil/sti/pdfs/ADA440979.pdf

[27] Miura, H., & Matsuo, A. Numerical simulation of solid propellant combustion in a gun chamber. Collection of Technical Papers - AIAA/ASME/SAE/ASEE 42nd Joint Propulsion Conference, 8(July), 6048–6067, 2006. https://doi.org/10.2514/6.2006-4955

[28] Woodley, C., Carriere, A., Franco, P., Nussbaum, J., Chabaux, X., & Longuet, B. Comparisons of internal ballistics simulations of 40mm gun firings. In 23rd International Symposium on Ballistics (pp. 359-367), 2007.

[29] Schoeffert, I. C. Simulation de la Ballistique Intérieure des canons, SIBIL. NT ETBS/CE/DMS/MMB/TDP N°06/86, 1986.

[30] Refloch, A., Courbet, B., Murrone, A., Villedieu, P., Laurent, C., Gilbank, P., Troyes, J., Tessé, L., Chaineray, G., Dargaud, J. B., Quémerais, E., & Vuillot, F. (n.d.). AL02-11 1 CFD Platforms and Coupling CEDRE Software

[31] Donea, J., Huerta, A., Ponthot, J. P., & Rodríguez-Ferran, A. (2004). Arbitrary Lagrangian–Eulerian Methods. Encyclopedia of computational mechanics

[32] Gibeling, H. J., & Buggeln, R. C. Reacting Flow Models for Navier-Stokes Analysis of Projectile Base Combustion. AIAA Paper No. 91-2077, 1991

[33] Menter, F. R. Zonal two equation κ-ω turbulence models for aerodynamic flows. AIAA 23rd Fluid Dynamics, Plasmadynamics, and Lasers Conference, 1993. https://doi.org/10.2514/6.1993-2906

[34] Klingenberg, G., & Mach, H. Investigation of combustion phenomena associated with the flow of hot propellant gases-I: Spectroscopic temperature measurements inside the muzzle flash of a rifle. Combustion and Flame, 27(C), 163–176. 1976. https://doi.org/10.1016/0010-2180(76)90020-1

[35] Zhang, H., Chen, Z., Jiang, X., & Li, H. Investigations on the exterior flow field and the efficiency of the muzzle brake. Journal of Mechanical Science and Technology, 27(1), 95–101. 2023. https://doi.org/10.1007/s12206-012-1223-8

[36] Westbrook, C., Creighton, J., Lund, C., & Dryer, F. A numerical model of chemical kinetics of combustion in a turbulent flow reactor. The Journal of Physical Chemistry, 81,25, 2542-2554. 1977. https://doi.org/10.1021/j100540a036

[37] Poinsot, T., & Veynante, D. Theoretical and Numerical Combustion. Third edition. 88 p, 2011

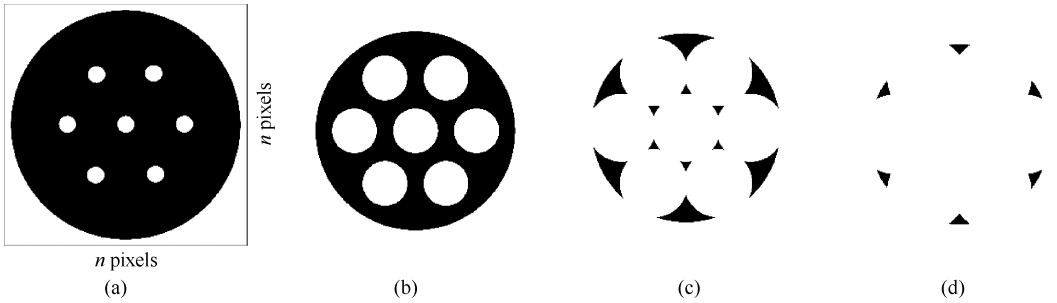

(a) (b) (c) (d)

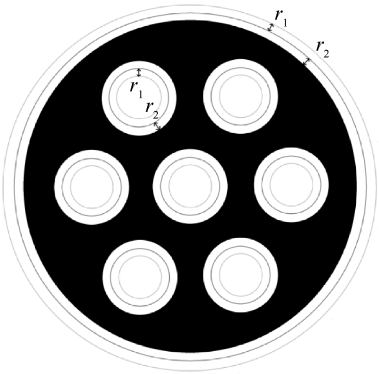

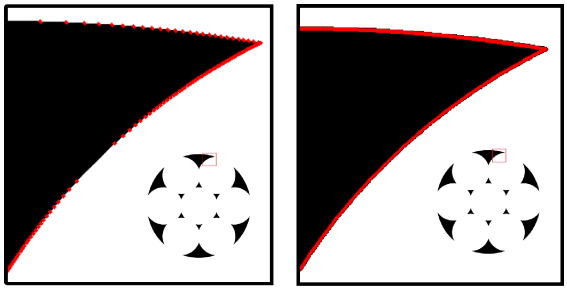

(a) (b)

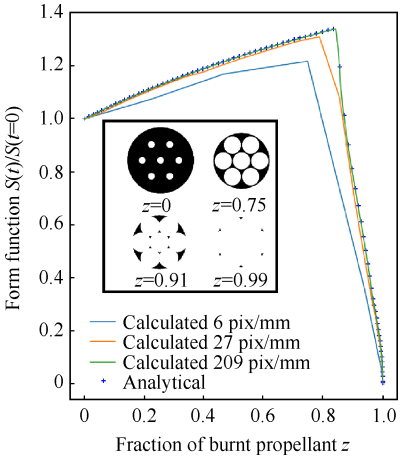

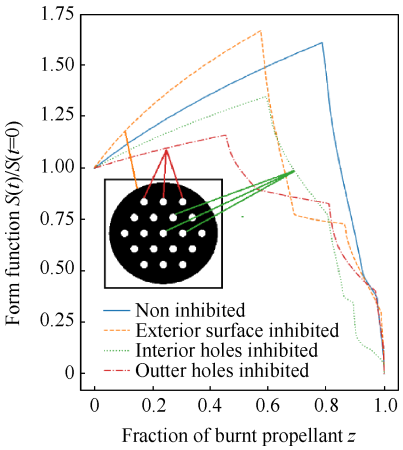

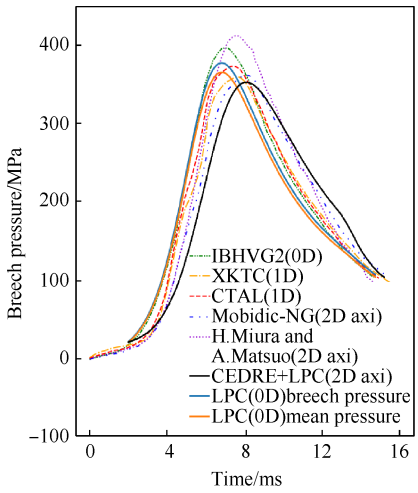

(a)

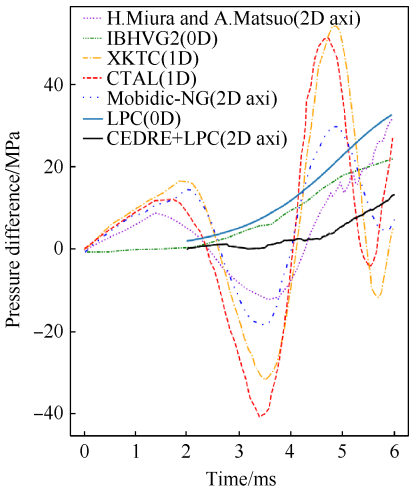

(b)

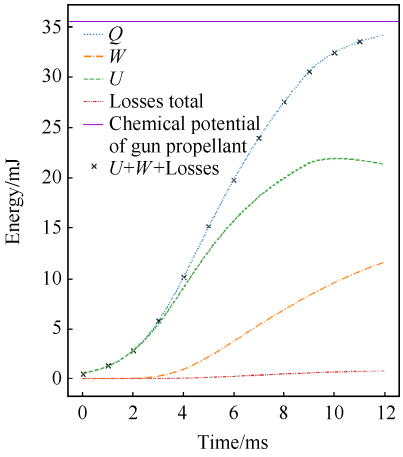

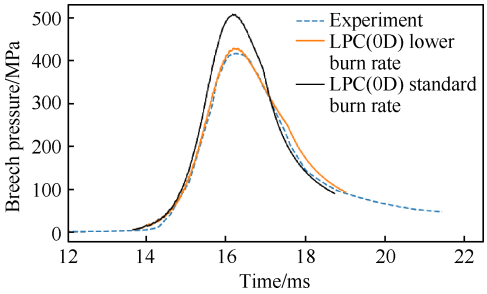

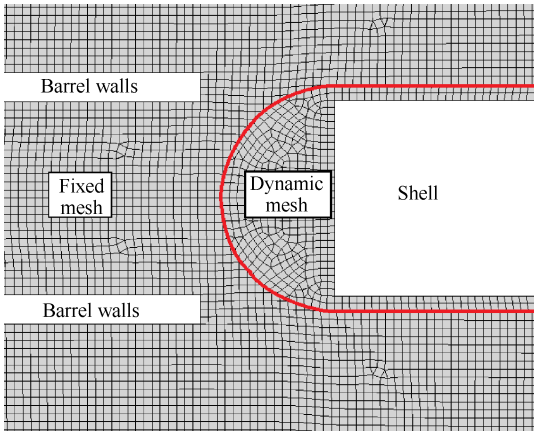

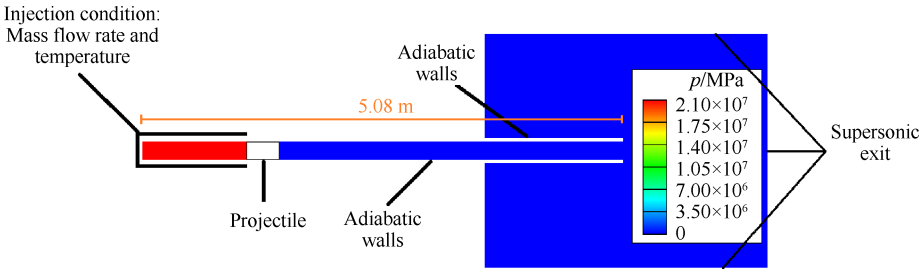

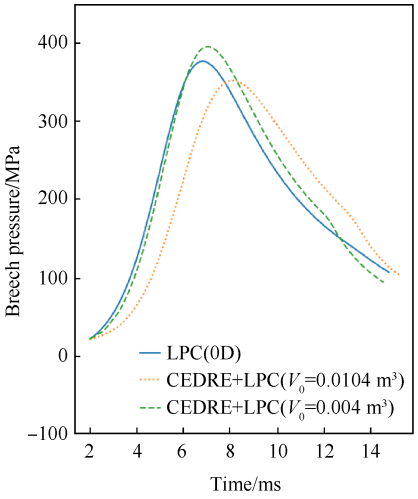

(a)

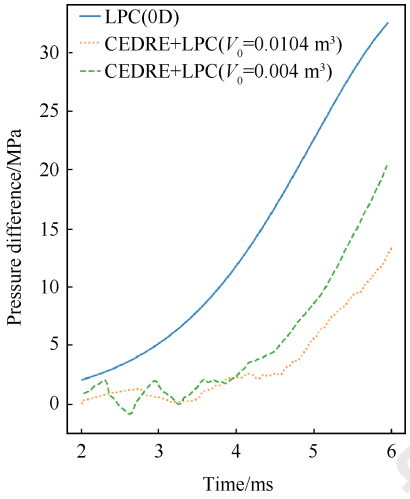

(b)

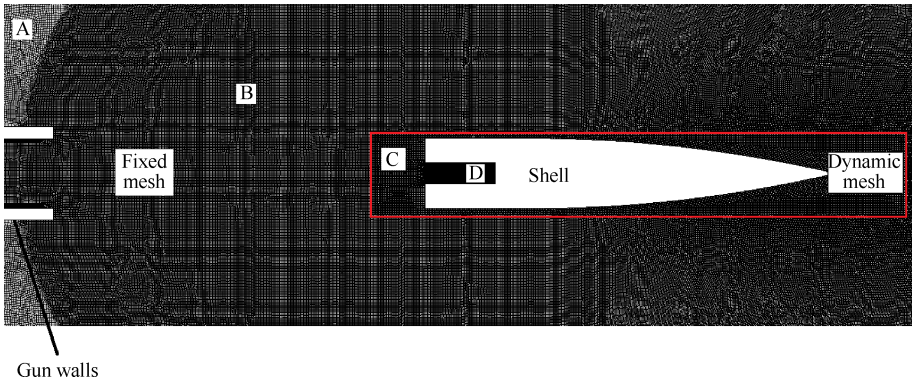

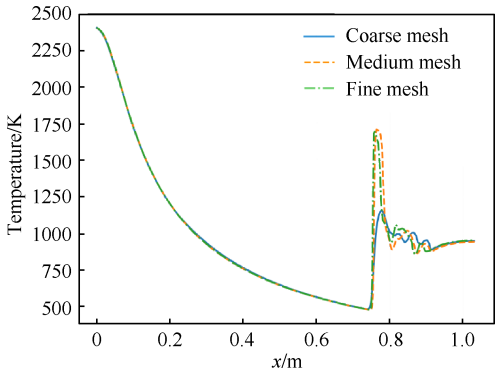

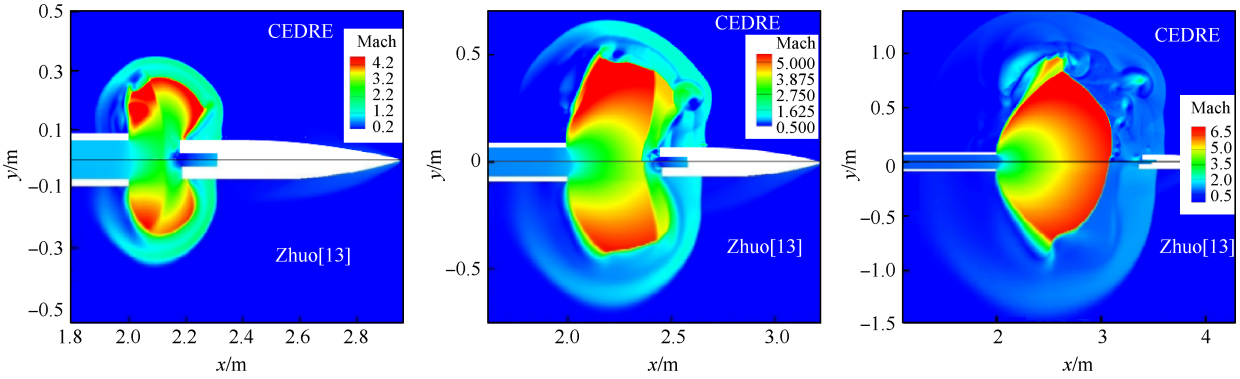

(a) (b) (c)

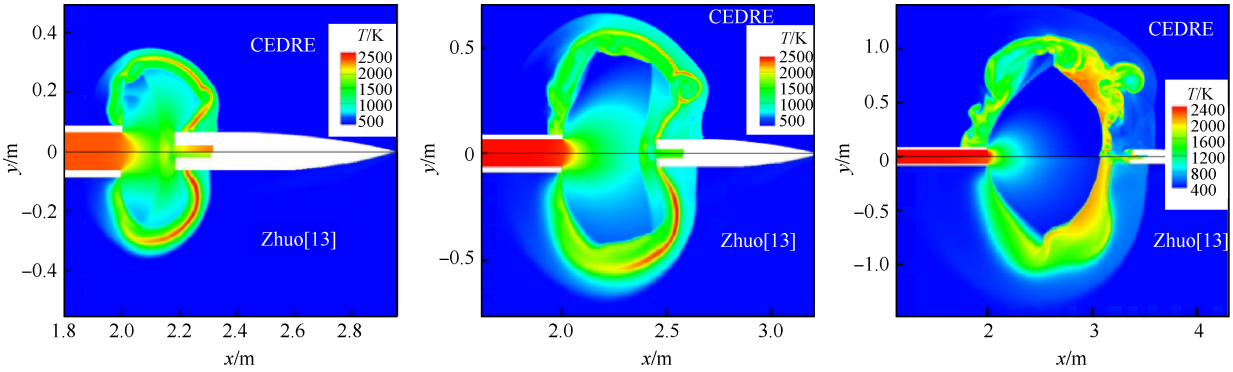

(a) (b) (c)

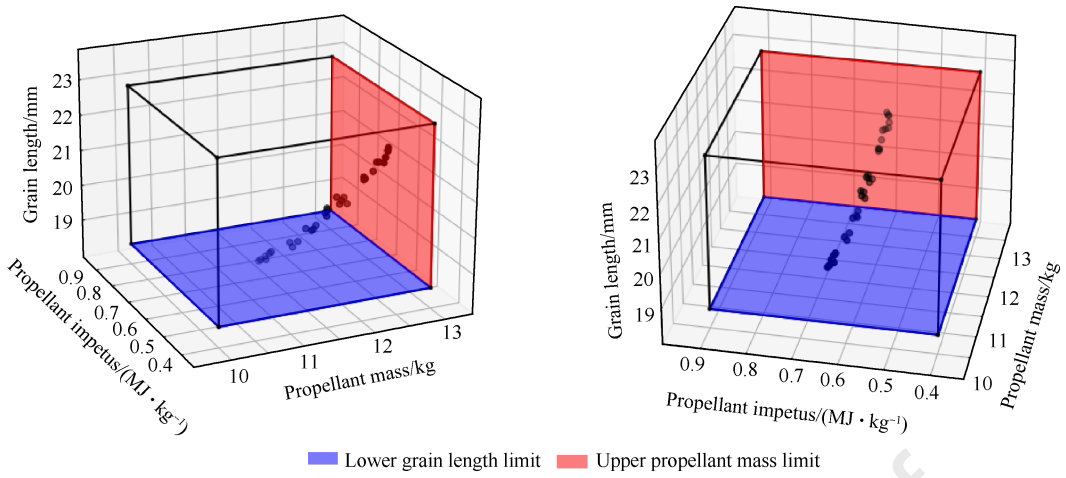

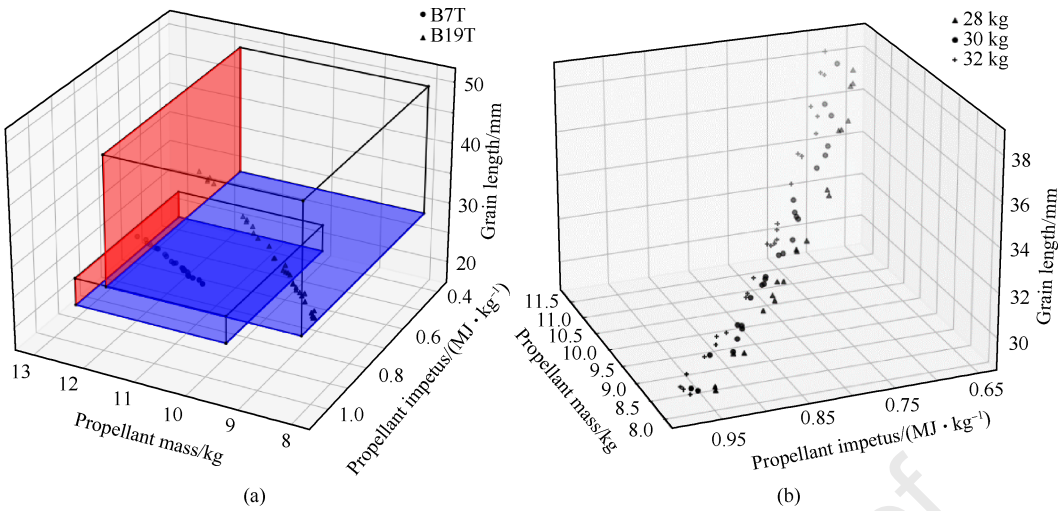

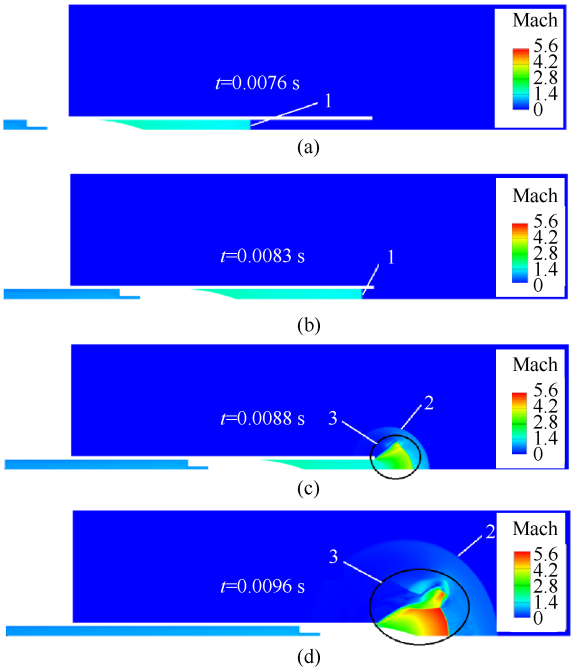

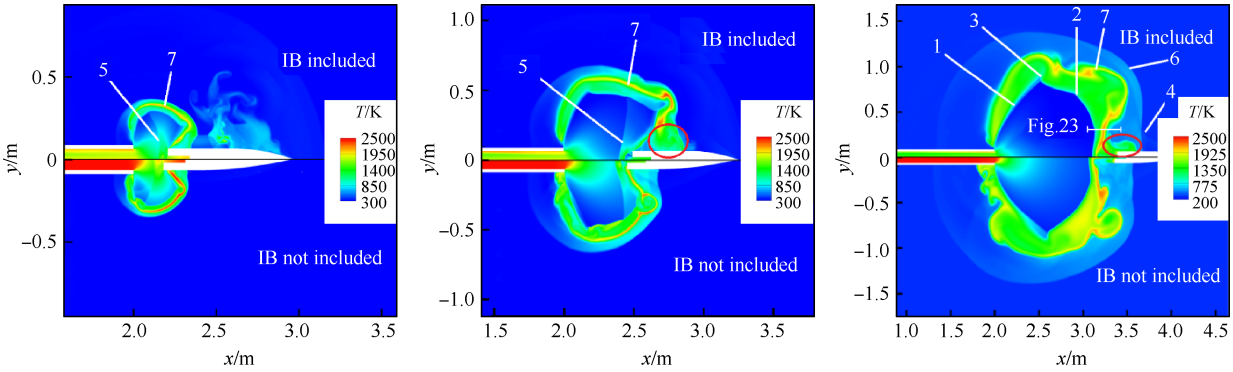

(a) (b) (c)

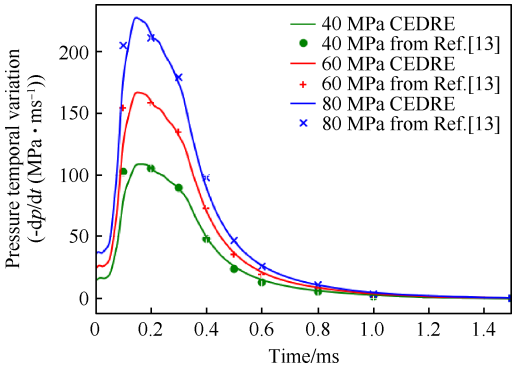

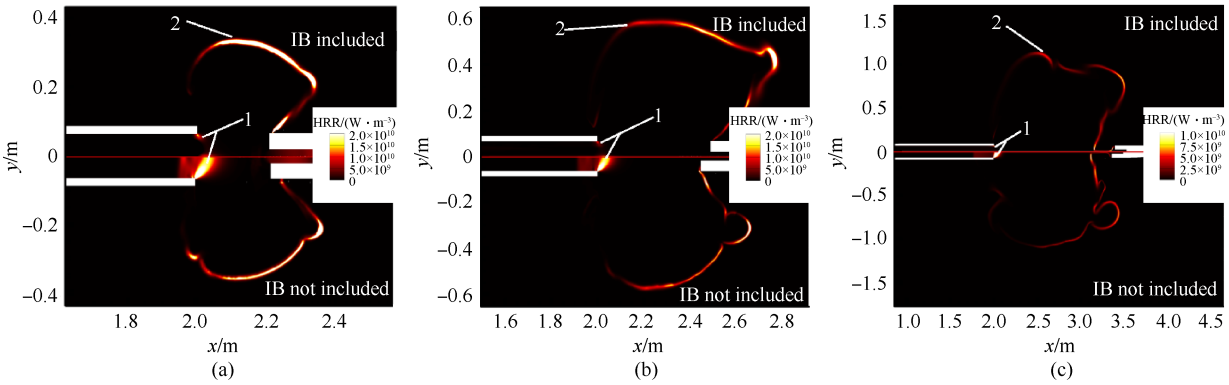

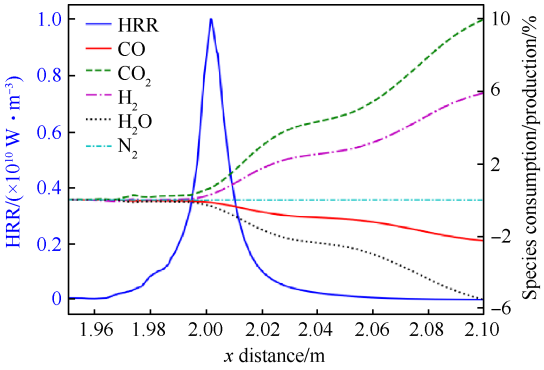

(a)

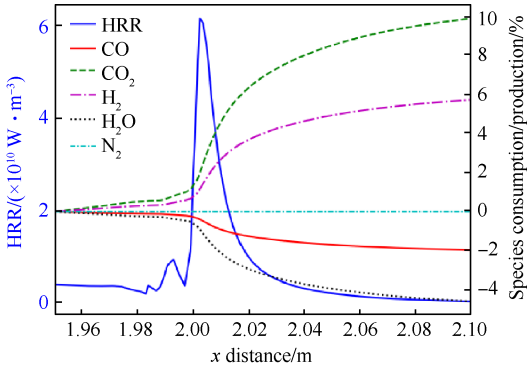

(b)

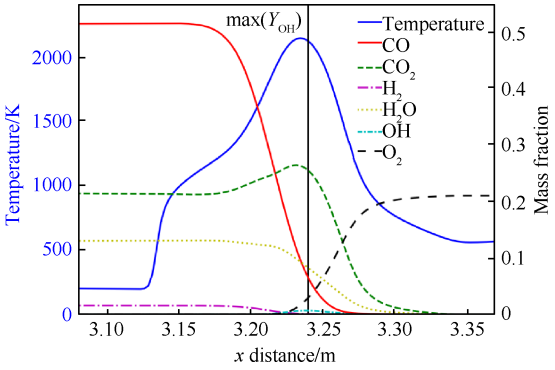

Declaration of Interest Statement

☒ The authors declare that they have no known competing financial interests or personal relationships that could have appeared to influence the work reported in this paper.

☐ The author is an Editorial Board Member/Editor-in-Chief/Associate Editor/Guest Editor for this journal and was not involved in the editorial review or the decision to publish this article.

☐ The authors declare the following financial interests/personal relationships which may be considered as potential competing interests: